UC Riverside
UC Riverside Electronic Theses and Dissertations

Title
Thermal Conductivity and Phonon Properties of Twisted Bilayer Graphene

Permalink
https://escholarship.org/uc/item/5zz2967q

Author
Li, Chenyang

Publication Date
2019

Peer reviewed|Thesis/dissertation

eScholarship.org Powered by the California Digital Library
University of California

UNIVERSITY OF CALIFORNIA
RIVERSIDE

Thermal Conductivity and Phonon Properties of Twisted Bilayer Graphene

A Dissertation submitted in partial satisfaction
of the requirements for the degree of

Doctor of Philosophy

in

Electrical Engineering

by

Chenyang Li

December 2019

Dissertation Committee:

Dr. Roger K. Lake, Chairperson
Dr. Alexander Balandin
Dr. Chen Xi

Copyright by
Chenyang Li
2019

The Dissertation of Chenyang Li is approved:

Committee Chairperson

University of California, Riverside

Acknowledgments

I would like to express my hear-felt gratitude and appreciation to my supervisor and mentor Roger K. Lake for his guidance, support and encouragement during past my four years. I have learned a lot from him about phonon transport, condensed matter physics, coding, scientific writing, data science and oral presentation. When I was struggling with my project, he saved me from giving up. He encouraged me that some one could spend one year for polishing one paper for the best story, why can not us just spend a few more weeks. Moreover, before being a PhD candidate, I was not comfortable with giving presentations, especially in front of many people. He strongly suggested and supported me to attend conferences and give oral presentations. After attending the APS March Meetings every year, both my presentation skill and confidence have been dramatically improved. It goes without saying that devoid of his constant support and guidance, none of the works appearing in the thesis would have ever been possible.

I also want to thank my committee member Prof. Alexander Balandin, for all the advice about my twisted bilayer graphene project. I have learned a lot about the experimental side of characterization from Dr. Balandin and his group.

Special thanks to my current lab mates in LATTE, Nima Djavid, In Jun Park, Rakibul Karim Akanda, Yuhang Liu and Topojit Denbath, as well as my former colleagues Dr. Mahesh Neupane, Dr. Bishwajit Debnath, Dr. Protik Das, Dr. Shanshan Su, Dr. Kuan Zhou, Dr. Supeng Ge and Dr. Yizhou Liu, for their help and support with many ideas, collaborative projects and enjoyable discussions. A special thanks to Amrit De from Physical Optics Corporation and Hong Ding from EsgynDB Corporation for their support during my summer intership.

On the personal side, I would like first to acknowledge my parents for their guidance and support for my higher education. Lastly, I would like to thank to my dear girl friend Xinran Wang for her love and great support.

The text of this dissertation, in part or in full, is a reprint of the material as it appears in the following journal and/or proceedings:

- Carbon [1]. Reprinted with permission from [1]. © [2018] ELSEVIER.
- Carbon [2]. Reprinted with permission from [2]. © [2019] ELSEVIER.

The co-author Roger K. Lake, listed in the above publications directed and supervised the research which forms the basis for this dissertation. The remaining co-authors listed provided technical expertise and support as collaborators.

This work was supported in part by the National Science Foundation under awards 1307671 and 1433395 and by FAME, one of six centers of STARnet, a Semiconductor Research Corporation program sponsored by MARCO and DARPA. Numerical simulations were supported in part by the Spins and Heat in Nanoscale Electronic Systems (SHINES) an Energy Frontier Research Center funded by the U.S. Department of Energy, Office of Science, Basic Energy Sciences under Award #DE-SC0012670. This work used the Extreme Science and Engineering Discovery Environment (XSEDE) [3] which is supported by National Science Foundation Grant No. ACI-1548562 and allocation ID TG-DMR130081. Used resources include Stampede-2 and Comet.

To my parents and dear girl friend Xinran Wang, love you forever.

ABSTRACT OF THE DISSERTATION

Thermal Conductivity and Phonon Properties of Twisted Bilayer Graphene

by

Chenyang Li

Doctor of Philosophy, Graduate Program in Electrical Engineering
University of California, Riverside, December 2019
Dr. Roger K. Lake, Chairperson

Misorientation of two layers of bilayer graphene leaves distinct signatures in the electronic properties and the phonon modes. The effect on the thermal conductivity has received the least attention and is the least well understood. In this work, the in-plane thermal conductivity of twisted bilayer graphene (TBG) is investigated as a function of temperature and interlayer misorientation angle using nonequilibrium molecular dynamics (NEMD). The central result is that with rotation angles larger than 13°, the calculated thermal conductivities decrease approximately linearly with the increasing lattice constant of the commensurate TBG unit cell. Comparisons of the phonon dispersions show that misorientation has negligible effect on the low-energy phonon frequencies and velocities. However, the larger periodicity of TBG reduces the Brillouin zone size to the extent that the zone edge acoustic phonons are thermally populated. This allows Umklapp scattering to reduce the lifetimes of the phonons contributing to the thermal transport, and consequently, to reduce the thermal conductivity. This explanation is supported by direct calculation of reduced phonon lifetimes in TBG based on density functional theory (DFT) for larger rotation angles.

Nothing was previously known about how small twist angles (<13°) affect the thermal conductivity of TBG, and how it approaches its aligned value as the twist angle approaches 0°. To provide insight into these questions, we performed large scale NEMD calculations on commensurate TBG structures with angles down to 1.87°. The results show a smooth, non-monotonic behavior of the thermal conductivity with respect to the commensurate lattice constant. As the commensurate lattice constant increases, the thermal conductivity initially decreases by 50%, and then it returns to 90% of its aligned value as the angle is reduced to 1.89°. These same qualitative trends are followed by the trends in the shear elastic constant, the wrinkling intensity, and the out-of-plane ZA_2 phonon frequency. The picture that emerges of the physical mechanism governing the thermal conductivity is that misorientation reduces the shear elastic constant; the reduced shear elastic constant enables greater wrinkling; and the greater wrinkling reduces the thermal conductivity. The small-angle behavior of the thermal conductivity raises the question of how do response functions approach their aligned values as the twist angle approaches 0°. Is the approach gradual, discontinuous, or a combination of the two?

Much attention has been given recently to the material data science. A particular emphasis is placed on low dimensional materials exhibiting novel electrical and thermal properties. An improved dimension classifier model has been created to identify the quasi-1D materials that are often classified within the 2D material family. The algorithm is based on the fact that quasi-1D materials contain different bond lengths within the unit cell. The model can identify known quasi-1D material based on the structural data from Material Project Database. Using the optimized distributed gradient boosting model (XGBoost),

both the band gap and the magnetization properties can be predicted from structural and elemental features. By fitting the XGBoost model with 15,000 kinds of materials, the accuracy of the predictions on the 5000 testing samples is greater than 91%. The mean absolute error of the band gap prediction is only 0.148 eV. Additionally, 1,025 kinds of magnetic materials have been identified among 5000 kinds of materials. According to the feature importance analysis, the most correlated feature for band gap prediction is the number of the valence electrons. While, for the magnetic material classification, it is the elemental period.

Contents

List of Figures

List of Tables

Chapter 1

Rationale

1.1 Objectives

As the first discovered 2D atomic crystal, graphene has been subject of intense investigations due to its promising electrical [8], mechanical [9] and optical properties [10]. The massless electrons of graphene due to their peculiar electronic structure guaranteed its high electrical conductivity [11]. And a good electrical conductor is always a good heat conductor. The excellent thermal characteristics were soon discovered by Balandin's group [12]. It is reported that at room temperature, the thermal conductivity of single layer graphene (SLG) can be as high as 5000 W/m·K. The extremely high thermal conductivity of graphene opens up a new line of research in thermal management applications. Researchers have great interest in heat dissipation and heat transport in graphene [13]. The mechanisms such as doping, isotope, defects and hydrogenation which can greatly affect thermal conductivity of SLG have been well studied. However, research on tuning the thermal conductivity of graphene-based materials has just begun.

Another graphene-based material, consisting of two SLG with a 0.34 nm Van-der-Waals (VdW) gap, named bilayer graphene (BLG) has attracted lots of attention in recent years. The unique characteristics have potential applications in next generation microprocessors [14]. The growing interest motivated people to study the phonon and thermal properties of BLG. Both experimental and theoretical studies show that due to the compressed ZA mode, the thermal conductivity of BLG is relatively lower than that of SLG [15, 16]. However, the thermal conductivity of BLG, which is approximately 2000 W/m·K [15], is still much higher than the conventional heat conductor. The interaction between the layers are VdW forces which are considerably weaker than the strong in-plane sp^2 bonding. The deviation of the phonon frequencies in BLG from SLG is negligible for the LA and TA acoustic branches. The only exception is the layer breathing mode, also called ZA$_2$. For BLG the ZA$_2$ mode has a very significant splitting with a frequency of 95 cm^{-1} [17] Moreover, using Raman spectroscopy, researchers observed multiple peaks between 100-200 cm^{-1} which can be associated with ZA$_2$ [18].

Currently, the interests of the physicists have been shifting to the twisted bilayer graphene (TBG), which is constructed by rotating one layer with a commensurate rotation angle. Although it is believed that rotation cannot strongly affect the interlayer interaction, the breaking symmetry of the Bernal stacking will result in captivating dependence of thermal conductivity on the commensurate rotation angle. In this thesis, we will uncover the commensurate rotation effect on the thermal conductivity of TBG. Also an underlying physical mechanisms will be presented by studying the phonon and elastic properties of TBG.

1.2 Organization

The rest of the dissertation is organized as follow: Chapter 2 presents the in-plane thermal conductivity of TBG as a function of temperature and commensurate rotation angle larger than 13°. Chapter 3 presents the answer to the question of how small commensurate rotation angles ($< 13°$) affect the thermal conductivity of TBG, and how it approaches its aligned value as the twist angle approaches 0°. Chapter 4 presents a comparison of interatomic potentials for TBG, both interlayer potentials and intralayer potentials will be considered. Chapter 5 presents preliminary work on machine learning: dimension classification, band gap prediction and magnetic material classification. Chapter 6 is a summary of all the interesting findings and an outlook for future work. In the Appendix, the band gap predictor by using machine learning and the dimension classifier are documented. Also, we did an analysis of the vibrational mode for BLG using Elastic continuum model.

Chapter 2

Lattice Constant Dependent Thermal Conductivity of Misoriented Bilayer Graphene

2.1 Introduction

The record high thermal conductivity of graphene has created widespread interest and may lead to its applications in thermal management [19,20]. The room temperature thermal conductivity (κ) of single layer graphene (SLG) is approximately $3000 - 5000$ W/m·K, while the room temperature thermal conductivity of few layer graphene (FLG) ranges from 1300 W/m·K to 2800 W/m·K [19, 21, 22]. Similar values have also been obtained from theoretical studies [23–25]. There are many factors that influence the thermal conductivity of graphene such as vacancies, chirality, isotope [26], wrinkles, number of layers, etc. Among them, the effect of interlayer misorientation on the in-plane thermal conductivity of bilayer graphene (BLG) has been the least studied, and it is the focus of this work.

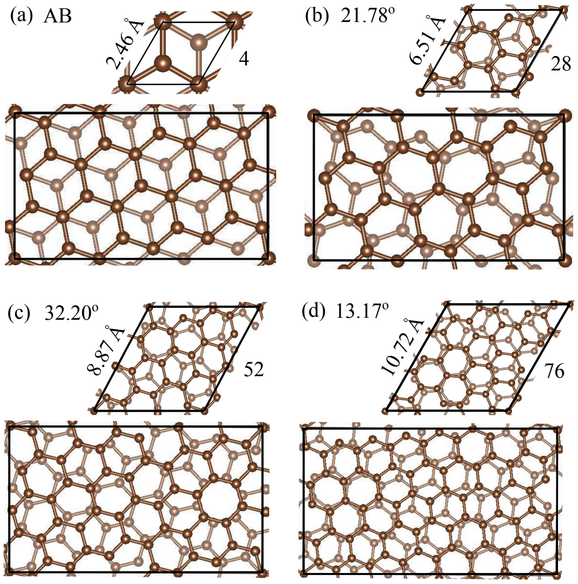

Figure 2.1: Top views of the primitive cells and the rectangular unit cells of (a) AB-BLG, (b) 21.78° m-BLG, (c) 32.20° m-BLG, (d) 13.17° m-BLG. The value of the primitive lattice constant is shown along the left edge of each primitive cell, and the number of atoms in each primitive cell is shown to the right of each cell.

In graphene, or BLG, heat is carried by the low-energy vibrational (phonon) modes [27]. Anything that alters the low-energy phonon spectrum or the phonon scattering can affect the thermal conductivity. Experimentally, Raman spectroscopy has been extensively used to probe the zone-center vibrational properties of graphene, AB-BLG, and misoriented BLG (m-BLG) [18,28–34]. It has been used to measure the misorientation angle dependence of the high-energy optical phonons of the G and 2D peaks of m-BLG, and it has also been used to measure the new peaks that appear in the low-energy range of 90–200 cm^{-1} in the vicinity of the original ZO′ breathing mode [18, 31, 35]. The position, intensity, and width of the Raman 2D peak can be used to identify the m-BLG misorientation angle [30, 33]. Misorientation also affects the electron-phonon interlayer and intralayer interactions [36, 37], and Raman spectroscopy has very recently been used to distinguish the interlayer from the intralayer interactions [37]. While the Raman studies are useful for understanding the optical phonon branches and their interactions with electrons, heat is carried by the low-energy acoustic modes over a range of wavevectors which the Raman studies do not probe.

Recently, the in-plane thermal conductivities of two suspended BLG samples were experimentally measured over a range of temperatures from 300 K to 650 K [15]. One sample was aligned AB stacked BLG (AB-BLG), and the other sample was misoriented-BLG (m-BLG) with a misorientation angle of 32.2°. The average κ values of the m-BLG were uniformly lower than those of the AB-BLG. There was considerable experimental uncertainty of the data, with error bars of up to 40%, and the measurements were taken from a single m-BLG sample. A theoretical study of m-BLG nanoribbons found strong edge effects and an increase of thermal conductivity for misorientation angles of 22.5° and 30.0° compared to that of an AB stacked nanoribbon [38]. Overall, the effect of the misorientation angle on the in-plane thermal conductivity of BLG is still an open question.

The existing computational research on the phonon properties of m-BLG indicates that misorientation only slightly affects the phonon frequencies, density of phonon modes and the specific heat above room temperature [17, 35, 39–41]. New low-energy $q = 0$ modes in the m-BLG $\omega - q$ dispersion naturally occur due to zone-folding. Considering the simple expression relating the thermal conductivity, specific heat, velocity, and effective mean-free path, $\kappa = \frac{1}{3}C_v \times v \times l_{\text{eff}}$, one would infer that interlayer misorientation should not significantly affect the in-plane thermal conductivity provided that l_{eff} is not significantly changed. However, zone-folding reduces the size of the Brillouin zone (BZ) and opens up new Umklapp scattering channels that result in increased Umklapp scattering and a reduced mean free path [15].

Usually, Umklapp scattering would be expected to have little effect on the heat transport by low-energy phonons with small wave vector q. The thermal conductivity depends on the low-energy region, while Umklapp processes dominate the high-energy region. However, the periodicity introduced by the moiré pattern or determined by the commensurate unit cell can be very long. The lattice constant of the commensurate unit cell with the smallest misorientation angle that we consider of 13.17° is 1.07 nm, corresponding to a BZ Γ-K path length of 3.91 nm^{-1}. At wave vector K, the phonon frequency of the LA branch is approximately 360 cm^{-1} corresponding to an energy of 45 meV, which is less than $2k_BT$ at room temperature [17]. Thus, the severe reduction of the BZ brings the zone edges into the low-energy range where Umklapp processes could play a role in the room temperature thermal transport.

2.2 Method and computational approach

The starting point of the theoretical investigation is the construction of the misoriented bilayer atomic structures using commensurate rotation angles. These special angles ensure that the overall structure remains periodic, albeit with a much longer periodicity.

Commensurate misorientation angles are given by [42]

$$\cos\theta = \frac{n^2 + 4nm + m^2}{2(n^2 + nm + m^2)}, \tag{2.1}$$

where m and n are non-negative integers with $m \leq n$. The commensurate unit cell vectors $\mathbf{c}_1$ and $\mathbf{c}_2$ are $\mathbf{c}_1 = n\mathbf{a}_1 + m\mathbf{a}_2$ and $\mathbf{c}_2 = -m\mathbf{a}_1 + (m + n)\mathbf{a}_2$. We will refer to $\mathbf{c}_1$ and $\mathbf{c}_2$ as the primitive lattice vectors, their magnitude as the primitive lattice constant, and a unit cell constructed with $\mathbf{c}_1$ and $\mathbf{c}_2$ as a primitive cell, since it is the smallest periodic cell that can be constructed for a given misorientation angle θ. Due to the 6-fold rotational symmetry of graphene, we only need to consider misorientation angles between 0° and 60°. The misorientation angles considered here are 0° (AB stacking), 13.17°, 21.78°, and 32.20°. The three angles were chosen since they give the three smallest primitive cells as shown in Fig. 2.1. A 27.79° primitive cell is the same size as the 32.30° primitive cell, but the 32.30° angle was chosen, since it corresponds to a clockwise rotation of the upper layer in the same sense as the 13.17° and 21.78° angles, and this is also the misorientation angle of the m-BLG sample measured in Ref. [15]. The next larger commensurate primitive cell corresponds to a rotation angle of 17.89° with a primitive lattice constant of 13.69 Å containing 124 atoms. The sizes of the commensurate primitive cells quickly increase from there, and a table of commensurate angles and primitive lattice constants is given in Ref. [43].

The NEMD simulations require a rectangular unit cell, so we define orthogonal unit cell vectors $\mathbf{r}_1$ and $\mathbf{r}_2$ as $\mathbf{r}_1 = \mathbf{c}_1$ and $\mathbf{r}_2 = 2\mathbf{c}_2 - \mathbf{c}_1$. The number of atoms N in the rectangular unit cell is $N = 8(n^2 + nm + m^2)$. A top view of the rectangular unit cells are shown in Fig. 2.1 underneath their respective primitive cells. The rectangular unit cell of AB-BLG can be made smaller than in Fig. 2.1a. It is constructed to be the same size as the 21.78° unit cell, so that the thermal conductivities can be compared at a constant width and a constant length. The rectangular unit cell is repeated multiple times in the direction of the heat transport. It is also repeated in the direction perpendicular to the direction of heat flow to ensure that the width is sufficiently large, so that the calculated thermal conductivity values are independent of the width [44].

For the NEMD simulations, the BLG structures are divided into $2N$ identical slabs along the transport direction where N is a positive integer, usually not less than 10 for the accuracy of calculation. We will refer to the slabs as 'NEMD slabs', since they are created purely for the NEMD calculation. For each NEMD slab, we obtain one statistical average temperature. The hot region is at the center in NEMD slab $N + 1$, and the cold regions are at the sample ends in NEMD slabs 1 and $2N$. The geometry is illustrated in the inset of Fig. 2.2b.

The NEMD simulations are implemented in the LAMMPS code [45]. The time step is 0.2 fs. A reactive empirical bond order (REBO) potential [46] is used for the in-plane bonding interactions, and the Lennard-Jones (LJ) potential is included for the interlayer van der Waals (vdW) forces with a well-depth energy of 2.96 meV and an equilibirum distance of 0.334 nm [47].

There are three steps to the simulation. The relaxation process (step 1) is a constant temperature, 340-ps-long, canonical-ensemble simulation that brings the system temperature up to 300 K as illustrated in Fig. 2.2a. We include a quantum correction [48] to the simulation temperature. The temperature of the BLG increases monotonically to 300 K during the first 150 ps; then the temperature fluctuates around 300 K. At 340 ps, the system

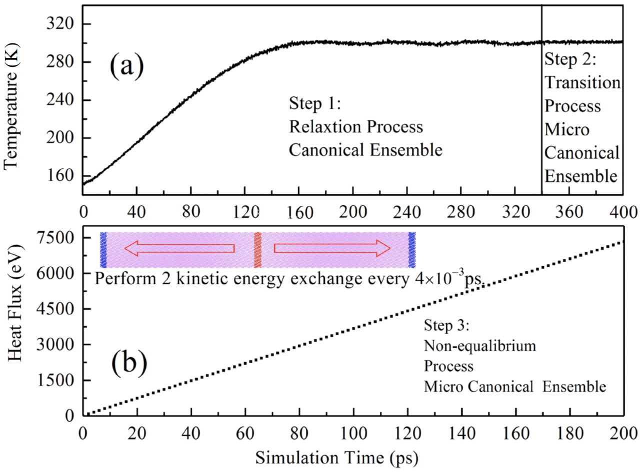

Figure 2.2: (a) Temperature as a function of simulation time during the relaxation process and the transition process of the NEMD simulation. The target temperature is $T = 300$ K and $\theta = 21.78°$. (b) Heat flux in the m-BLG as a function of simulation time during the non-equilibrium process. Inset: structure geometry showing the hot (red) and cold (blue) reservoirs and direction of heat flow (arrows).

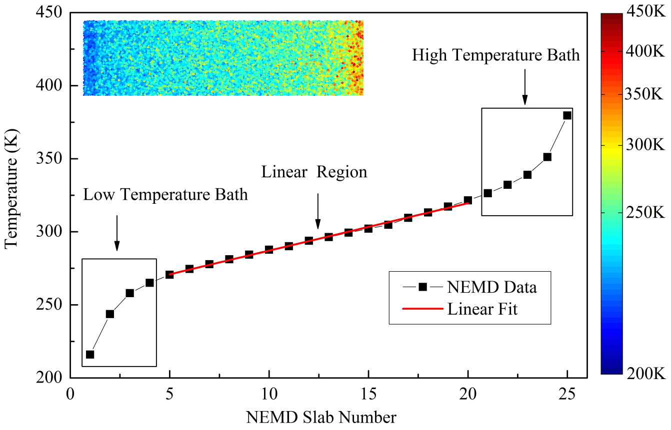

Figure 2.3: Temperature as a function of NEMD slab number for the left-half of the structure during the non-equilibrium process, for $\theta = 21.78°$ m-BLG at 300 K. The thermal conductivity is extracted from the slope in the linear region. Inset: color plot of temperature distribution of each atom. Temperatures are given by the color bar at right.

reaches a steady temperature of 300 K which indicates that the system is ready to enter the transition process (step 2). The transition process is a 60 ps, constant-energy simulation that ensures that the temperature of the system will maintain an average value of 300 K under a microcanonical ensemble. After the transition process, the system is ready to enter the non-equilibrium process for calculation of the thermal conductivity.

A heat flux J is applied by performing twice the kinetic energy exchange every 4 fs between the cold regions at the ends and the hot region in the middle according to the Müller-Plathe algorithm [49], as shown in the inset of Fig. 2.2b. The average temperature remains at 300 K. Fig. 2.2b shows the total heat flow as a function of simulation time for the 21.78° m-BLG. The linear dependence of total heat flux indicates that the heat flow is steady and smooth. The instantaneous J is the slope of the line in Fig. 2.2b.

Fig. 2.3 shows the temperature distribution and temperature gradient of the 21.78° m-BLG at 300 K. The inset is the temperature distribution of each atom in the BLG. The average temperature of the atoms in each NEMD slab is plotted underneath. The temperature profile shows non-linear regions (the high temperature and low temperature baths) and linear region. The temperature in the linear region, is centered around 300 K. The gradient of the linear part gives the temperature gradient ΔT.

With the values for ΔT and J, the thermal conductivity κ_L' is given by Fourier's law,

$$\kappa_L' = -\frac{J}{2A \cdot \Delta T}. \tag{2.2}$$

The factor of 2 in the denominator appears, because the heat flux is divided into two directions. The 'prime' on κ_L indicates that this value is extracted from a finite length simulation domain. A is the cross-sectional area (width × thickness) of the heat conduction direction. For bilayer graphene, a thickness of 6.68 Å is used for all samples, since the interlayer distance is insensitive to stacking or misoreintation [50]. Since all the simulations have the same fixed rate of kinetic energy exchange, J is a constant among all samples.

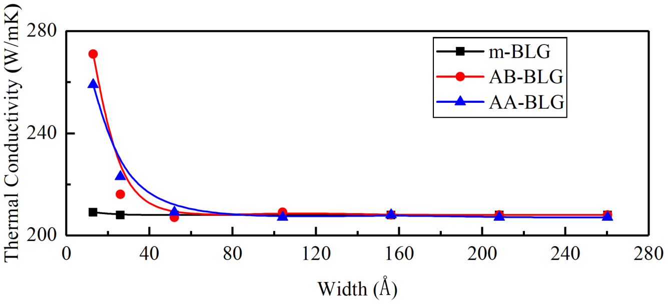

Figure 2.4: Thermal conductivity of 21.78° m-BLG, AB, and AA BLG as a function of width and at $T = 300$ K.

To ensure that the width is sufficiently large, the thermal conductivity is calculated as a function of the width. Fig. 2.4 shows the width dependence of the thermal conductivity κ'_L at $T = 300$ K for the AA, AB, and 21.78° structures all in the 21.78° geometry with constant length of 20 nm. The thermal conductivity of all three BLGs is higher at very small widths. Narrow widths result in reduced phonon-phonon scattering due to the lack of phonon-phonon combinations that satisfy the energy and momentum conservation rules for scattering [51]. The thermal conductivity at $T = 300$ K becomes width independent for widths greater than ~ 60 Å, and the converged value is approximately 210 W/m·K for all three structures. For temperatures above 300 K, increased phonon-phonon scattering reduces the phonon mean free path [52], so that the thermal conductivity at higher temperatures is also converged and independent of the width for widths ≥ 60 Å.

For each misorientation angle, 5 different lengths are simulated to obtain length-dependent values for the thermal conductivity κ'_L. These values are subsequently used to obtain a linear best fit to the inverse-length-dependence expression of the thermal conductivity [53],

$$\frac{1}{\kappa'_L} = \frac{1}{\kappa_L} + \frac{b}{L_z}. \tag{2.3}$$

In Eq. (2.3), b is the size coefficient. When plotted versus $1/L_z$, the intercept, $1/\kappa_L$, gives the length-converged thermal conductivity κ_L for $L_z \to \infty$. For all rotation angles including 0°, the width of the structure is ~ 60 Å and the length is varied from 200 Å to 2710 Å. The largest structures contain approximately 1.5×10^5 atoms.

To analyze the evolution of phonon dispersion and phonon group velocity, we apply the fluctuation dissipation theory implemented in the Fix-phonon package of the LAMMPS

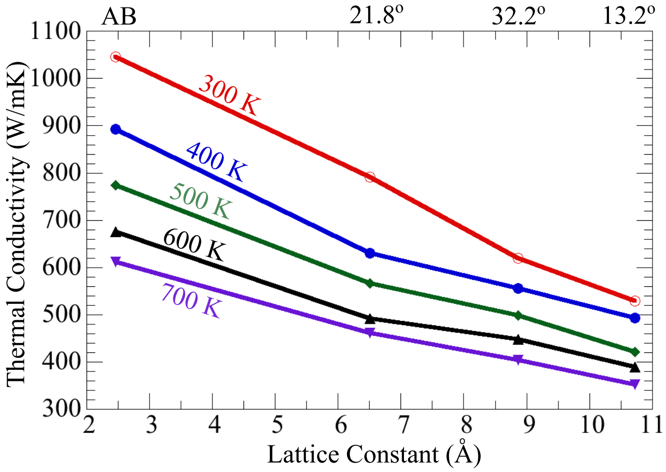

Figure 2.5: Lattice thermal conductivity of AB-BLG, 21.78° m-BLG, 32.20° m-BLG and 13.17° m-BLG plotted as a function of the primitive commensurate lattice constants for 5 different temperatures. The corresponding misorientation angles are labelled on the upper horizontal axis.

code, which has been demonstrated to produce accurate phonon dispersions [54, 55]. The hybrid potential combining both the REBO potential and the LJ potential is used as in the NEMD simulations. To avoid negative phonon frequencies near Γ, we use a $25 \times 25 \times 1$ supercell for all of the m-BLG as well as the unrotated AB-BLG. Since the unit cell has at least 28 atoms, the total number of iterations to enforce the acoustic sum rule is set at 50. All settings are the same as those used in the NEMD simulations.

As part of the assessment of the hybrid potential, we also calculated the phonon dispersion of AB-BLG using density functional theory (DFT) and compared the results to those from the LAMMPS calculations. DFT combined with ShengBTE [56] are also used to obatin the interatomic force constants (IFCs) of both BLG and m-BLG to determine phonon lifetimes. Details of the DFT simulations are provided in the Appendix.

2.3 Results and discussion

Fig. 2.5 is the central result of this work. It shows the in-plane lattice thermal conductivity κ_L obtained from Eq. (2.3) as a function of the primitive lattice constant of the different commensurate rotation angles for 5 different temperatures. For the range of angles considered, the thermal conductivity monotonically decreases as the size of the commensurate primitive cell increases. This trend of decreasing thermal conductivity with increasing commensurate primitive lattice constant is reminiscent of the trend observed in the interlayer electrical conductance as a function of lattice constant [43, 57–59]. However, the physics and the functional dependence are different. The physics of the electrons in m-BLG is determined by the misalignment of the K-points in the two layers. However, the low-energy phonons reside at Γ, and the Γ points of the two layers are always aligned. What does qualitatively explain the dependence of the lattice thermal conductivity on the commensurate primitive lattice constant is the reduction of the commensurate BZ and a consequent increase in Umklapp scattering within the low-energy range contributing to the thermal transport. This physical mechanism was previously suggested [15], and it is consistent with the trends resulting from the NEMD simulations.

The relationship between the phonon modes, the BZ, and the thermal conductivity is given by the Boltzmann transport equation [56]

$$\kappa = \frac{1}{N\Omega} \sum_{q,\lambda} \frac{\partial f}{\partial T} (\hbar\omega_\lambda) \nu_\lambda \nu_\lambda \tau_\lambda, \tag{2.4}$$

where N is the number of q points in the BZ, Ω is the volume of the unit cell, f is the Bose-Einstein distribution function, ω_λ is the phonon frequency of mode λ, ν_λ is the phonon group velocity along a certain direction, and τ_λ is the phonon lifetime. Fig. 2.6 shows

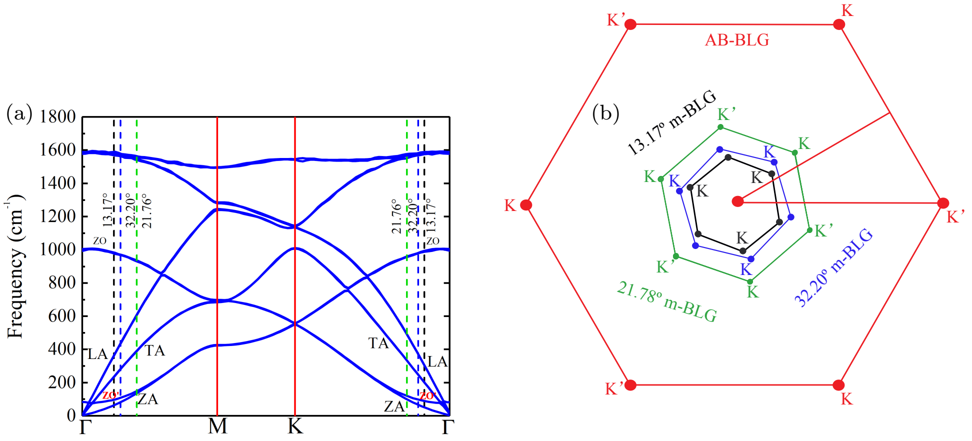

Figure 2.6: (a) Phonon dispersion of AB stacked bilayer graphene. The vertical dashed lines show the BZ edges of the m-BLGs corresponding to the misorientation angles as labelled. (b) BZs of AB-BLG, 21.78° m-BLG, 32.20° m-BLG, and 13.17° m-BLG. The high symmetry lines in the AB-BLG BZ are also shown.

the molecular dynamics (MD) calculated phonon dispersion of AB-BLG within the original BZ of the 4-atom AB-BLG primitive cell. The dashed vertical lines labelled 13.17°, 32.20° and 21.76° show the edges of the commensurate BZs of the corresponding m-BLGs. At the vertical line labeled 32.20° along the Γ-M path, the ZA, TA, and LA modes have energies of 10 meV, 35 meV, and 53 meV, respectively. Thus, the zone-edge energies of the m-BLG acoustic modes are less than k_BT (ZA) or $2k_BT$ (TA, LA), and Umklapp scattering can now reduce the lifetimes of the low-energy phonons relevant to thermal transport. For reference, the BZs of AB-BLG, 21.8° m-BLG, 32.20° m-BLG, 13.17° and the high symmetry lines of the AB-BLG BZ are shown in Fig. 2.6(b).

The other factors that govern the thermal transport are the phonon velocities and phonon energies. If misorientation reduces the phonon velocities, then this will reduce the thermal conductivity. To understand the effect of misorientation on the phonon velocities and energies, we compare the AB-BLG phonon frequencies and the m-BLG phonon frequencies calculated using the supercell of the m-BLG. By calculating the phonon frequencies of AB-BLG using the same lattice vectors as those of the m-BLG, we can directly compare the two phonon dispersions and separate out the effects of zone folding from misorientation. Fig. 2.7 shows side-by-side comparisons of AB-BLG and m-BLG with misorientation angles of 21.78°, 32.2°, and 13.17°. For each angle, visual inspection shows no difference between the phonon dispersions of the AB-BLG and the m-BLG. All of the new energies appearing at the high symmetry points are the result of zone folding. Furthermore, the slopes of the the bands, i.e. the phonon group velocities, also appear to be the same. Quantitative values for the LA and TA phonon velocities at Γ, numerically calculated from the dispersion curves, are given in Table 2.1. The quantitative values are unaffected by misorientation.

Since the phonon velocities and energies are unaffected by misorientation, the only explanation consistent with the trend of reduced thermal conductivity with increased m-BLG lattice constant is that it is the result of increased scattering among the low-energy thermal phonons. To provide further support for this hypothesis, we calculate the phonon lifetimes for AB-BLG and 21.78° m-BLG and compare them in Fig. 2.8. The phonon lifetimes of the LA branches of AB-BLG and m-BLG are similar for low energies below the energy of the ZO' mode of ~ 83 cm^{-1}. Above this energy, the lifetimes of the m-BLG LA mode are less than the lifetimes of the AB-BLG LA mode. In this same energy range, the lifetimes of the TA and ZA modes of m-BLG are less than those of AB-BLG. The reduced phonon lifetimes of m-BLG compared to those of AB-BLG provides further support to the

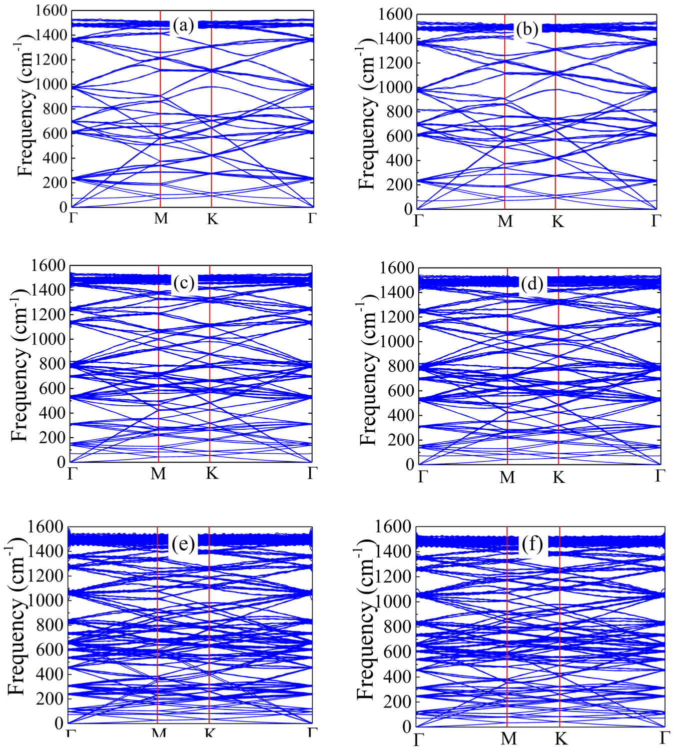

Figure 2.7: Phonon dispersion of (a) AB-BLG calculated using the 21.78° m-BLG lattice constants, (b) 21.78° m-BLG, (c) AB-BLG calculated using the 32.20° m-BLG lattice constants, (d) 32.20° m-BLG, (e) AB-BLG calculated using the 13.17° m-BLG lattice constants, and (f) 13.17° m-BLG.

hypothesis of increased Umklapp scattering in m-BLG as the cause of the reduced thermal conductivity.

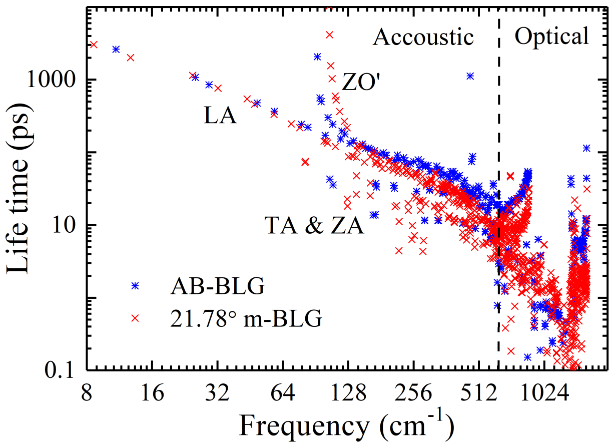

Figure 2.8: Phonon lifetime comparison of AB-BLG and 21.78° m-BLG at 300 K.

Table 2.1: Comparison between AB-BLG, 21.78°, 32.20° and 13.17° m-BLG phonon group velocity around Γ for LA and TA modes.

Misorientation Angle(°)	υ_{LA}(km/s)	υ_{TA} (km/s)
0° AB-BLG	20.0	12.9
21.78° m-BLG	20.0	12.8
21.78° AB-BLG	20.0	12.9
32.20° m-BLG	20.1	12.9
32.20° AB-BLG	20.0	12.9
13.17° m-BLG	20.0	12.8
13.17° AB-BLG	20.0	12.9

2.4 Conclusion

The dependence of the in-plane BLG lattice thermal conductivity on the interlayer misorientation angles 13.17°, 21.78° and 32.20° is theoretically investigated using NEMD simulations for temperatures ranging from 300 K to 700 K. The thermal conductivities decrease approximately linearly with the increasing lattice constant of the commensurate m-BLG unit cell. At $T = 300$ K, the thermal conductivity decreases by a factor of 2.0 between AB-BLG and 13.2° m-BLG. For the 3 misorientation angles considered, misorientation does not affect the phonon velocities or energies, but it does reduce the Brillouin zone size to the extent that the zone edge acoustic phonon energies are thermally populated at room temperature and above. This allows Umklapp scattering to reduce the lifetimes of the phonons contributing to the thermal transport and, consequently, to reduce the thermal conductivity. DFT calculations do find a reduction of the phonon lifetimes in m-BLG compared to AB-BLG.

Appendix

This appendix describes the assessment and verification of the potentials and NEMD method used in the calculations, and it also provides the details of the DFT calculations. At room temperature (300 K), the value of κ_L for single layer graphene extracted from our NEMD simulations is 2116 W/m·K which is within the experimental range of values [15]. Additionally, our value for κ_L of AB-BLG at room temperature extracted from the NEMD simulations is 1046 W/m·K, which is lower, but still close to the experimental

Table 2.2: Comparisons of the AB-BLG phonon frequencies at the Γ, M, and K points, calculated from MD using the hybrid REBO and LJ potentials, from our DFT calculations, from prior DFT calculations (in units of cm^{-1}), and from prior experimental measruement (EXP) ^{a}Reference [4], ^{b}Reference [5], ^{c}Reference [6], ^{d}Reference [7].

Method	Γ			K					M				
	LO	ZO	ZO′	LA	TA	ZA	LO	TO	LA	TA	ZA	LO	TO
MD	1589	993	83	1140	1007	553	1144	1543	1286	684	427	1286	1494
DFT	1571	869	92	1210	994	530	1211	1356	1325	628	474	1344	1401
DFT^a	1560	884	78	1210	997	532	1228	1327	1318	627	473	1360	1396
EXP	1590^b	861^b	–	1184^c	–	482^c	1184^c	1313^d	1290^d	630^b	465^b	1321^d	1389^d

results.

A well known artifact of NEMD simulations of the thermal conductivity is that they are sensitive to the finite size effect [27,44,60–63]. A length dependent study of NEMD simulations of SLG required a length of 16 μm for the thermal conductivity to reach a value of 3200 W/mK [62]. This is the longest length simulated and correspondingly highest value for the thermal conductivity obtained from a NEMD simulation of SLG. A detailed examination of the finite size effect in both the direct approach (NEMD) and in the Green-Kubo method is described in Ref. [60]. There, it is shown that extrapolating Eq. (2.3) to the $1/L_z = 0$ intercept gives a good comparison between the two methods and the experimental values for Si. A comprehensive tabulation of values from different studies can be found in Ref. [64]. The NEMD approach systematically underestimates the thermal conductivity.

Since, in this work, the simulation domains are similar for all of the misorientation angles, the systematic underestimation will not affect the trends, which are the focus of the study. We only ask whether the misorientation increases or decreases the thermal conductivity with respect to the unrotated structure. For this question, the NEMD simulations are sufficient to capture the trends, just as they capture the correct temperature trends.

For verification of the potentials, we calculated the known phonon dispersion of AB-BLG using DFT. The DFT calculations are performed using the generalized gradient approximation (GGA) with Perdew-Burke-Ernzerhof (PBE) parametrization [65] for the exchange correlation functional, as implemented in Vienna Ab-initio Simulation Package (VASP) [66, 67]. Van der Waals corrections are included with the semiempirical DFT-D2 Grimme's method [68, 69]. The structure is relaxed until the forces were less than 10^{-5} eV/. A plane-wave basis set with kinetic energy cutoff of 500 meV is used to expand the electronic wave functions and a 16 × 16 × 2 Monkhorst Pack k-point mesh is adopted for the integration over the first BZ. The optimized lattice parameter of the unit cell is 2.46 Å, which is in good agreement with experiment [70] and theory [4]. The phonon dispersion is calculated for a 5 × 5 × 1 supercell using Phonopy [71].

Quantitative comparisons of the phonon frequencies of AB-BLG at high symmetry points calculated from MD, DFT, as well as the prior theoretical [4] and experimental results of others [5–7] are shown in Table 2.2. Since previous theoretical calculations of AB-BLG are also obtained from DFT, our DFT results match closely with the prior DFT studies [4]. The largest differences between the MD results and the DFT results occur in the high energy optical modes Γ_{ZO} and K_{TO} which are not relevant to this work. The MD acoustic branch energies are within 5% of the DFT results at K and within 10% of the DFT results at M.

The phonon lifetimes τ_λ of AB-BLG and m-BLG are calculated from the scattering rates as implemented in ShengBTE [56], $\frac{1}{\tau_\lambda} = \frac{1}{N}(\sum_\lambda \Gamma_{absorb} + \frac{1}{2}\sum_\lambda \Gamma_{emission})$, where the quantities Γ_{absorb} and $\Gamma_{emission}$ are the three-phonon scattering rates, obtained by perturbation theory. These phonon scattering rates depend on phonon frequencies, atomic masses, and IFCs [56]. The second-order and third-order IFCs are calculated using DFT. In the calculation of the IFCs, we use $5 \times 5 \times 1$ and $3 \times 3 \times 1$ supercells for BLG and m-BLG, respectively. The q-point mesh is set to $40 \times 40 \times 1$ and $15 \times 15 \times 1$ for BLG and m-BLG, respectively. Interactions up to the fourth nearest neighbours are included for calculating the anharmonic (third-order) force constants.

Acknowledgements

This text of this chapter is in full of a reprint of the material as it appears in the Carbon journal. [1] This work was supported in part by the National Science Foundation under awards 1307671 and 1433395 and by FAME, one of six centers of STARnet, a Semiconductor Research Corporation program sponsored by MARCO and DARPA. This work used the Extreme Science and Engineering Discovery Environment (XSEDE) [3] which is supported by National Science Foundation Grant No. ACI-1548562 and allocation ID TG-DMR130081. Used resources include Stampede-2 and Comet.

Chapter 3

Elastic Constant Dependent Thermal Conductivity of Small Angle Bilayer Graphene

The effect of layer misorientation on the electronic structure and the electrical conductance of bilayer graphene (BLG) and multi-layer graphene has received much attention [43, 57, 59, 72–77], and interest was recently renewed by the experimental discovery of superconductivity at certain low misorientation angles [78, 79] where the electronic bands become flat at the Fermi level [74, 75]. Experimentally, the effect of interlayer rotation on the phonon spectrum has been probed extensively with Raman spectroscopy [18, 28–35, 37]. Theoretical research on the phonon properties of twisted bilayer graphene (TBG) finds that the phonon frequencies, density of phonon modes, phonon velocities, and specific heats of the low frequency phonon branches vary little with the interlayer rotation angle [1, 17, 35, 39, 40].

Bringing these two different lines of research together, recent theory proposes a phonon driven mechanism for the superconductivity [80]. The effect of misorientation on the in-plane thermal conductivity of TBG has received less attention [1, 15, 38, 81, 82]. The one experimental study on the in-plane thermal conductivity of TBG carried out opto-thermal measurements [27] on one TBG sample with a twist angle of $\sim 32^\circ$, and found that interlayer misorientation reduced the in-plane thermal conductivity by up to 50% [15].

Standard expressions for the thermal conductivity based on the phonon Boltzmann transport equation show that the lattice thermal conductivity depends on the phonon velocities, frequencies, and lifetimes. Since misorientation has little effect on the phonon velocities and frequencies, it was proposed that that the zone-folding that occurs in TBG opens up new channels for phonon scattering that are unavailable in unrotated BLG [15]. As a consequence, the phonon lifetimes are reduced, which results in a reduction in the thermal conductivity. A recent theoretical study of the of the lattice thermal conductivity of TBG with three rotation angles corresponding to the three smallest commensurate unit cells, 21.78°, 32.17°, and 13.17°, found that the thermal conductivity decreased approximately linearly as the commensurate lattice constant increased [1]. The scaling of the thermal conductivity with the lattice constant rather than the angle was consistent with the hypothesis that the decreased thermal conductivity in TBG resulted from increased scattering allowed by the large zone-folding in the reduced Brillouin zones [15].

However, the three angles considered in [1] give only a small picture within the total range of possible misorientation angles. What happens at smaller misorientation angles of 10° or less is still an open question. It seems reasonable to expect that as the rotation angle is reduced towards zero, the thermal conductivity might return to its aligned value in some smooth manner even though the commensurate lattice constant becomes very large. If this expectation were true, then there would be a minimum in the thermal conductivity as a function of the commensurate lattice constant. Such a non-monotonic dependence of the thermal conductivity on the commensurate lattice constant would suggest that physical mechanisms other than increased scattering allowed by reduced Brillouin zones play a role in governing the thermal conductivity. To investigate the mechanisms that govern the thermal conductivity in TBG, and to provide insight into the physical mechanisms that give rise to the angle and lattice constant dependence of the thermal transport, we perform large-scale non-equilibrium molecular dynamics calculations of the thermal conductivity of TBG for commensurate twist angles down to 1.89°, we calculate the elastic constants and the phonon spectra for the misoriented structures, and we compare the results to those from other theoretical and experimental works.

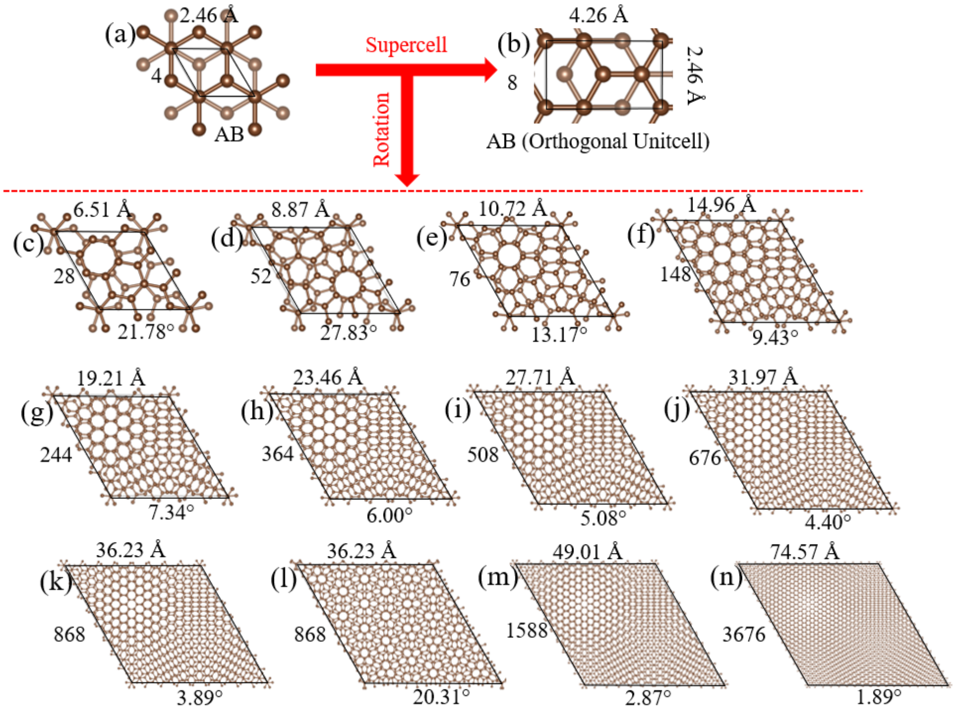

Figure 3.1: (a) and (c-n) The primitive cells of AB-BLG and commensurate TBG. For each primitive cell, the rotation angle is given along the bottom edge, the number of atoms are shown along the left edge, and the commensurate lattice constant is given along the top edge. (b) A rectangular unit cell created and then repeated for constructing the long ribbons for the thermal transport calculations.

3.1 Methods

The approach used to create the commensurate unit cells and to model their thermal conductivities was previously described in detail [1], and only a brief description of the most important points is provided here. A total of 13 different commensurate rotation angles are considered with their commensurate primitive cells shown in Fig. 3.1. For each structure, the rotation angle, lattice constant, and number of atoms in the commensurate primitive cell are shown. The sizes of the commensurate primitive cells quickly increase as the rotation angle decreases, and at the smallest angle of 1.89°, the primitive cell contains 3676 atoms. All of the angles chosen fall along the curve of minimum commensurate primitive cells shown in Fig. 2 of Shallcross et al. [73], except for the one angle of 20.31°. The primitive commensurate cells for 20.31° and 3.89° have the same primitive commensurate cell lattice constants, even though their moiré patterns look very different. The misoriented primitive cells for all of angles that fall along the curve of minimum commensurate primitive cells appear to smoothly transition from a region of AB stacking to a region of AA stacking. For the 20.31° structure, there are many such transitions within the primitive cell. This angle is included to test whether the physics governing the thermal conductivity is determined by the rotation angle or the size of the primitive commensurate cell. If the physics is governed by the rotation angle, then the thermal conductivities for misorientations of 3.89° and 20.31° should be very different. If the physics is governed by the size of the commensurate primitive cell, then the thermal conductivities should be the same.

Calculations of the phonon dispersions and thermal conductivities are performed using molecular dynamics (MD) and non-equilibrium molecular dynamics (NEMD) [49] as implemented in LAMMPS [45]. Detailed benchmarking of various interatomic potentials has been reported for graphene [83], but there are no equivalent benchmarking studies for bilayer graphene. The common intralayer potentials include Tersoff [84, 85], Brenner [86], the reactive empirical bond order potential (REBO) [46, 87], and the long-range bond-order potential for carbon (LCBOP) [88]. All of these potentials belong to empirical bond order potentials (EBOPs) [89] and treat electronic binding as effective pairs. For bilayer graphene and misoriented bilayer graphene, the long range interlayer potential is critical. To model this, a long range interlayer potential is added to the above intralayer potentials, and it generally takes the form of a Lennard-Jones (LJ) potential [87]. Most recently a new interlayer potential, dihedral-angle-corrected registry-dependent interlayer potential (DRIP), was created specifically for misoriented multilayer graphene [90]. Calculations presented here used REBO for the intralayer potential, which is the most recent extension originating from the Tersoff potential, with the two types of interlayer potentials, LJ, as implemented in the adaptive intermolecular REBO (AIREBO) potential, and DRIP. All calculations are performed with AIREBO, and the main result, the trend in the thermal conductivity, is verified with REBO+DRIP.

The thermal conductivity is calculated using non-equilibrium molecular dynamics (NEMD) implemented in LAMMPS [45], in which a constant small heat flux is applied across the simulation domain and the gradient of the average temperature directly gives the thermal conductivity. The average temperature for all calculations is $T = 300$ K. For calculation of the thermal conductivity using this direct approach, the primitive cells shown in Fig. 3.1 are expanded into rectangular cells, and the rectangular cells are then repeated in both length and width to form long ribbons for the simulation domain. Periodic boundary conditions are used in the width direction so that there are no edges and no edge effects. When we refer to the “width” of the ribbon, we are referring to the width of the central ribbon to which we apply periodic boundary conditions.

Finite width and finite length effects are both present, and they are addressed using the following approaches. The thermal conductivity of ribbons of increasing width are simulated until the thermal conductivity (κ_l) becomes independent of the width. The width at which this occurs is ~ 70 Å as shown in Fig. 3.2(a). All of the simulated structures have a width greater than 70 Å. The widths slightly vary, since the ribbons must be constructed from integer multiples of the primitive cells shown in Fig. 3.1.

To address the finite length effect, for each angle in Fig. 3.1, multiple ribbons are constructed of increasing length L ranging from 20 nm to 12.9 μm. The largest ribbon contains $8,359,232$ atoms. The inverse of the calculated thermal conductivity $\frac{1}{\kappa'_L}$ for each length is plotted versus $1/L$ and fit to the line $\frac{1}{\kappa'_L} = \frac{1}{\kappa_L} + \frac{b}{L}$ [53]. As shown in Fig. 3.2, the dependence of $\frac{1}{\kappa'_L}$ on $\frac{1}{L}$ is linear. The intercept at $\frac{1}{L} = 0$ gives the converged value of κ_L as $L \to \infty$.

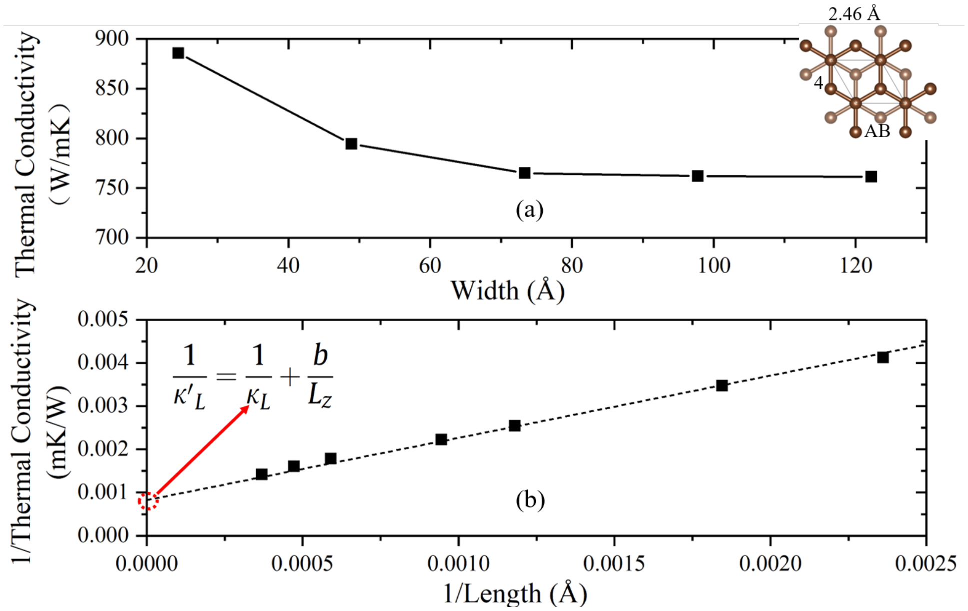

Figure 3.2: Lattice thermal conductivity of AB-BLG plotted as a function of (a) width and (b) inverse length. The length of the ribbon in (a) is 1.06 μm and the width of the ribbon in (b) is 7.87 nm.

Phonon dispersions are calculated using the Fix-phonon package of the LAMMPS code [54]. In this approach the dynamical matrix is constructed directly from the time averaged displacement-displacement correlation function evaluated during the molecular dynamics simulations. The dynamical matrix constructed in this manner is temperature dependent, and all simulations are performed at a temperature of $T = 300$ K. To avoid negative phonon frequencies near Γ, we use $25 \times 25 \times 1$ supercells for all structures. The resulting supercell sizes range from 17,500 atoms (AB) to 2,229,750 atoms (1.89°). The total number of iterations to enforce the acoustic sum rule is set at 50. All settings are the same as those used in the NEMD simulations. Velocities of the three acoustic branches are determined by evaluating the derivatives, $v = \frac{\partial \omega}{\partial q}\Big|_{q \to 0}$.

The elastic constants are obtained by introducing small deformations of the crystal cell around the equilibrium configuration and solving

$$\frac{\delta E}{V_0} = \frac{1}{2}\sum_{ij,kl} C_{ij,kl}\epsilon_{ij}\epsilon_{kl}, \quad \text{and} \quad \epsilon_{ij} = \frac{1}{2}(\frac{\partial \delta x_i}{\partial x_j} + \frac{\partial \delta x_j}{\partial x_i}) \tag{3.1}$$

where i, j, k, l are deformation directions in three dimensions, $C_{ij,kl}$ is the elastic constant, V_0 is the equilibrium volume of the relaxed structure, and δE is the potential difference recorded at each timestep. The Voigt form for the elastic constants will be used in the results and discussion; for example C_{44} is the Voigt notation for $C_{23,23}$.

The out-of-plane wrinkling intensity is quantified with the unitless metric $\gamma = (\eta_A/\eta_\lambda) \times 100\%$, where η_A is the mean wrinkling amplitude and η_λ is the mean wrinkling wavelength [91]. η_A is obtained by the averaging the standard deviation of out-of-plane coordinates of every atom in each layer, $\eta_A = \frac{1}{2}\sum_{l=1}^{2}\sqrt{\frac{1}{N}\sum_{i=1}^{N}(z_{i,l} - \bar{z}_l)^2}$, where l denotes the layer number, N is the total number of atoms, $z_{i,l}$ is the out-of-plane coordinate of atom i in layer l, and $\bar{z}_l$ is the average out-of-plane coordinate of layer l. The wrinkling wavelength η_λ is determined from the Fourier transform of z_i along the heat transfer direction, $\frac{1}{N}\sum_{j,l}(z_{j,l} - \bar{z}_l)e^{ikx_{j,l}}$, where $x_{j,l}$ is the x coordinate of atom j in layer l.

3.2 Results

The calculated room-temperature thermal conductivities for all of the misorientation angles shown in Fig. 3.1 are plotted versus their commensurate primitive-cell lattice constants in Fig. 3.3. The corresponding rotation angles are shown next to each data point. The first 4 points with the smallest lattice constants have a decreasing linear dependence on the commensurate lattice constant, as previously reported [1]. However, this trend abruptly ends at a commensurate lattice constant of 1.1 nm (13.17°), where the thermal conductivity reaches a minimum value. For commensurate lattice constants larger than 1.1 nm, the thermal conductivity monotonically increases with increasing lattice constant and returns towards the value of the unrotated AB-BLG.

For the chosen angles below 13°, the commensurate lattice constants monotonically increase as the angles decrease. However, two very different angles, 3.89° and 20.31° have identical commensurate lattice constants, and their thermal conductivities are also identical. This result provides strong evidence that the thermal conductivity of TBG is a function of the commensurate lattice constant rather than the twist angle. To further support that contention, we show the thermal conductivities plotted versus rotation angle in the inset of Fig. 3.3.

The calculations in Fig. 3.3 were performed with the AIREBO (REBO+LJ) potential. To verify that the above trend is not an artifact of the interlayer LJ potential, we performed a subset of the above calculations using REBO with the interlayer potential recently developed specifically for twisted multilayer graphene, DRIP. The results are shown in Fig. 3.7 in the Appendix. The trends remain the same, with a minimum thermal conductivity occurring at the commensurate lattice constant of 1.1 nm.

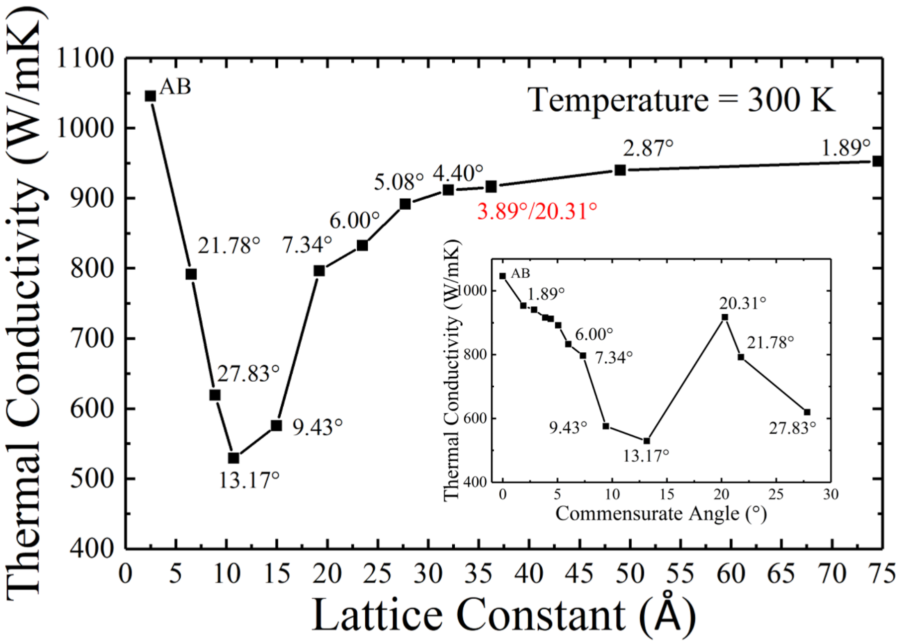

Figure 3.3: Lattice thermal conductivity of AB-BLG and TBG plotted as a function of the primitive commensurate lattice constant. The corresponding misorientation angles are shown for each data point. The inset shows the same data plotted versus twist angle.

From the phonon Boltzmann transport equation [56], $\kappa_l = \frac{1}{N\Omega}\sum_{q,\lambda}\frac{\partial n}{\partial T}(\hbar\omega_\lambda)\nu_\lambda\nu_\lambda\tau_\lambda$, two other factors that affect the thermal conductivity are the low-energy phonon frequencies and velocities. There are 6 low energy phonon branches that originate from the 3 original acoustic branches, longitudinal (LA), transverse (TA), and out-of-plane (ZA), of each individual graphene layer. We will refer to the 3 acoustic branches that go to zero frequency in the BLG and TBG structures as the LA, TA, and ZA modes and the three that have finite frequency at Γ as the LA_2, TA_2 and ZA_2 modes. We use notation consistent with Refs. [64, 92], but we note that the ZA_2 mode is often referred to as the ZO' mode in the literature describing Raman spectroscopy measurements [31, 93]. The phonon velocities for the LA and TA phonon branches were previously calculated for angles down to 7.34° [17]. We now calculate their velocities for angles down to 1.89°, and we find that over the entire range of angles, the velocities only vary in the fourth significant digit. The velocities of the LA modes lie in the range of 20.03–20.09 km/s, and the velocities of the TA modes lie in the range of 12.83–12.86 km/s. Thus, the velocities of these two modes play no role in explaining the changes in the thermal conductivity with misorientation.

The out-of-plane ZA modes in the individual graphene layers strongly couple and split in frequency when the two layers are brought together to form BLG or TBG. The Γ point frequency of the ZA_2 mode with AB stacking calculated from LAMMPS is 82.5 cm^{-1}. Fig. 3.4 shows the Γ point frequency of the ZA_2 mode, ω_{ZA_2}, plotted versus the commensurate lattice constant. The dependence of the frequency on the commensurate lattice constant follows the same trend as that of the thermal conductivity. The mode initially softens, it reaches a minimum frequency at the commensurate lattice constant of 1.1 nm, and then it begins to harden as the commensurate lattice constant increases. The ZA_2 frequencies for 3.89° and 20.31° are identical indicating a dependence on the commensurate lattice constant rather than on the angle. While the consistency of this trend is interesting, it cannot explain the trends in the thermal conductivity, since the ZA_2 mode is not expected to play a significant role in thermal transport.

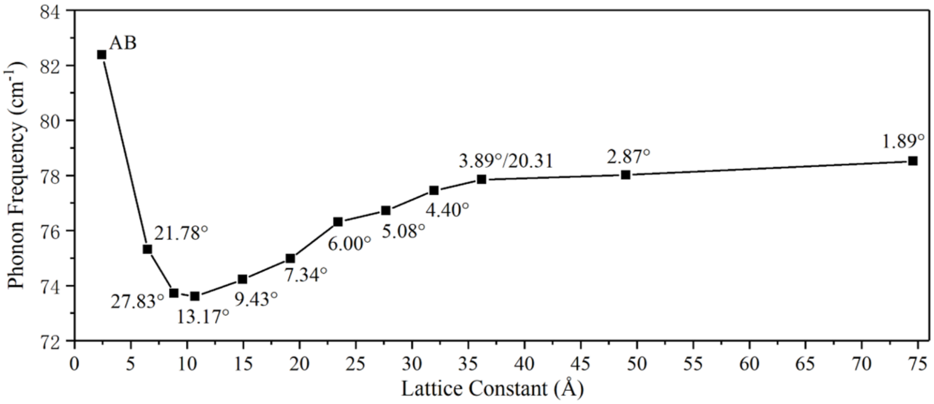

Figure 3.4: Commensurate lattice constant dependence of the Γ point frequency of the ZA_2 mode.

Since the presence of wrinkles can reduce the thermal conductivity by up to 80% [91, 94], and, furthermore, wrinkling will always be present [95], we investigate the wrinkling of the TBG structures. Fig. 3.5(a) shows a snapshot of the 13.17° structure during the heat transfer calculation. Out-of-plane fluctuations or wrinkling are apparent in the cross-sectional view. To quantify the intensity of the wrinkling, we plot the unitless metric γ (described in Methods) as a function of the commensurate lattice constant in Fig. 3.5(b). The wrinkling intensity peaks at the commensurate lattice constant of 1.1 nm corresponding to the minimum in the thermal conductivity. The qualitative trends in the wrinkling intensity track those of the thermal conductivity. The thermal conductivity is lowest when the wrinkling intensity is highest.

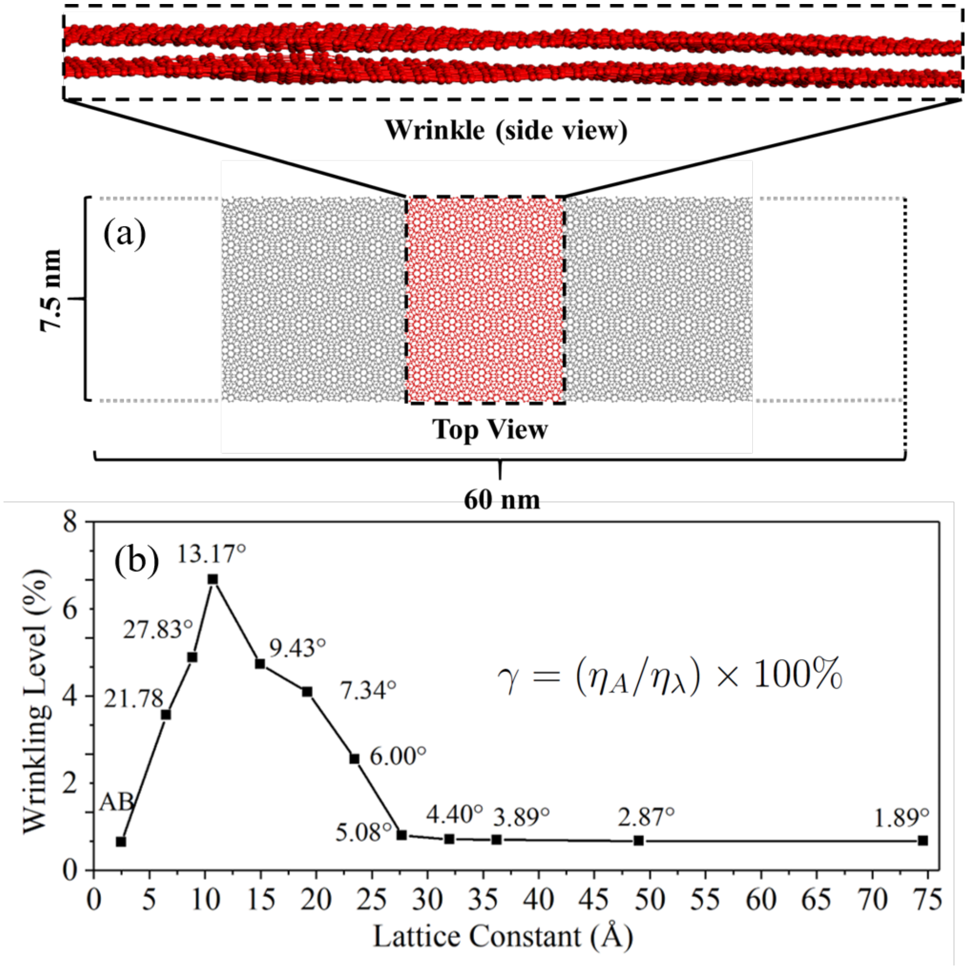

Figure 3.5: (a) Snapshot of the cross section and top view of the 13.17° structure during the NEMD simulation. Out-of-plane spatial fluctuations or wrinkling are present. (b) Wrinkling intensity γ as a function of commensurate lattice constant.

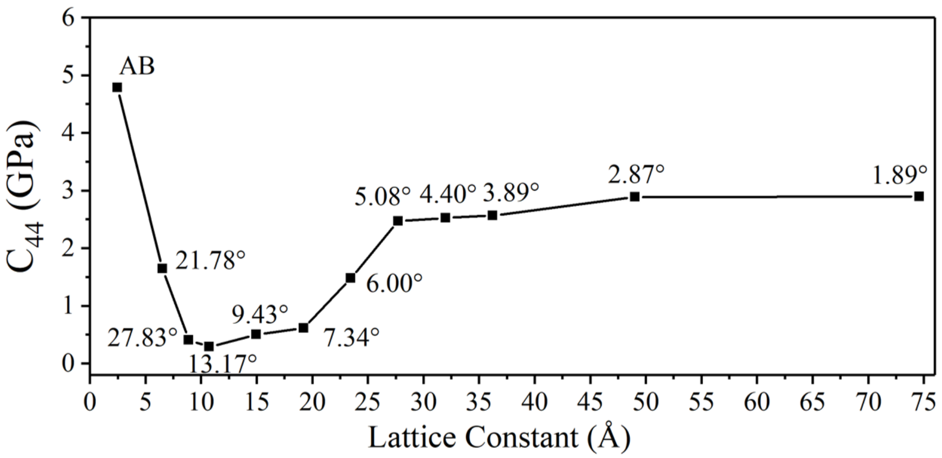

Figure 3.6: Elastic constant C_{44} plotted versus the commensurate lattice constant.

The ease with which BLG can bend or wrinkle depends on the shear elastic constant C_{44} [96]. Therefore, we calculate C_{44} for the structures shown in Fig. 3.1, and plot the values versus commensurate lattice constant in Fig. 3.6. The trend in C_{44} matches the trends in the thermal conductivity and the wrinkling intensity. For AB-BLG, $C_{44} = 4.8$ GPa, and this agrees with other experimental and theoretical values as shown in Table 3.1. C_{44} reaches a minimum value of 0.293 GPa at the misorientation angle of 13.17° with a commensurate lattice constant of 1.1 nm, and then it returns to 2.9 GPa at the smallest angle of 1.89° with a commensurate lattice constant of 7.5 nm. C_{44} decreases by a factor of 16 between the maximum and minimum value. At the smallest rotation angle, it is below the AB aligned value by a factor of 1.6. The calculated numerical values for all angles are given in Table 3.1. Table 3.1 also includes calculated values for C_{11}, C_{12}, and C_{33}, along with experimental and theoretical values from other works. As shown in Table 3.1, only C_{44} is affected by interlayer misorientation.

3.3 Discussion

The picture that emerges from the above results is that the interlayer misorientation reduces the shear elastic constant C_{44} which increases the wrinkling of the TBG. The increased out-of-plane wrinkling then reduces the thermal conductivity. The three parts of this mechanism, reduced C_{44}, increased wrinkling, and reduced thermal conductivity, are consistent with prior results in the literature. The reduction in C_{44} with misorientation is consistent with previous experimental studies on Kish graphite [97] and pyrolitic graphite [98] and a theoretical study of turbostratic graphite [96]. The theoretical study provides a clear description of how a reduction in C_{44} reduces the energy for out-of-plane wrinkling [96]. Experimental measurements found that the average thermal conductivity of graphene with wrinkles is 27% lower than that of wrinkle-free graphene [94]. NEMD-AIREBO simulations found that a 10% wrinkling intensity in single layer graphene resulted in a 20% decrease in the thermal conductivity and a 20% intensity led to an 80% decrease [91]. Therefore, all of the required mechanisms that drive this process are well-established and validated in the literature.

There have been two previous calculations of the thermal conductivity of TBG [38,82]. Both studies used LAMMPS with an optimized Tersoff-LJ potential, small structure sizes (5 nm × 13 nm) [38] (10 nm × 22 nm) [82], incommensurate rotation angles, and open boundaries in the width direction. The last two items make comparisons with our results problematic. Because of the open boundaries, the transport was dominated by the edges of the nanoribbons [38,82], which, because of the incommensurate angles, change as a function of the rotation angle. In [38], the thermal conductivity decreased as the rotation angle increased from 0° (AB) to 15°. Then, the thermal conductivities of 22.5° and 30° were larger than that of 0° with the maximum occurring at 30°. In [82], the thermal conductivity monotonically decreased as the rotation angle increased from 0° (AA) to 20°, and then a local maximum occurred at 30°. The pattern was mirror symmetric as the angle decreased from 60° (AB). The maximum values occurred for AA and AB stacking, and they were equal. In both studies, a 30° rotation caused one layer to have a zigzag edge and the other layer to have an armchair edge. The relatively smooth edges gave rise to the maximum (or local maximum) values of the thermal conductivities [38, 82]. However, the presence of angle dependent edge effects prevents meaningful comparisons with our results, since it is not clear how much of the thermal conductivity reduction was due to edge effects and how much was due to other processes.

Previous calculations of C_{44} found a one-order-of-magnitude drop from 4.8 GPa to 0.274 GPa as the commensurate lattice constant increased from 2.46 Å (AB) to 6.51 Å (21.78°) [96]. As the lattice constant increased further, C_{44} gradually declined to a minimum average value of 0.2 GPa at a commensurate lattice constant of 2.56 nm corresponding to a rotation angle of 11.0°. The calculations were performed using density functional theory (DFT).

Prior calculations of the ZA_2 frequency found a drop from 95 cm^{-1} to 89.5 cm^{-1} as the commensurate lattice constant increased from 2.46 Å (AB) to 6.51 Å (21.78°) [17]. After the initial decrease, there was a slight monotonic decline to 89.1 cm^{-1} as the commensurate lattice constant was increased to 1.9 nm corresponding to a misorientation angle of 7.34°. These calculations used the Born-von Karman (BvK) model for the intralayer forces and the LJ potential for interlayer forces.

One significant difference between our NEMD and MD simulations and the BvK model or DFT calculations is that our simulations explicitly take into account finite temperature effects and time-dependent thermal fluctuations. DFT is a zero-temperature theory. In the BvK approach, there is no relaxation of the structure so that the geometry of the layers remains ideally flat. In our NEMD and MD calculations, the effects of finite temperature and out-of-plane wrinkling are included both in the thermal conductivity calculations and in the construction of the dynamical matrix for the calculations of the phonon spectra.

What is unique to our results is the prediction of non-monotonic behavior of the thermal conductivity with respect to the commensurate lattice constant. For the small angle rotations, the commensurate lattice constants become extremely large. Our calculations of the thermal conductivity, C_{44}, and ω_{ZA_2} all show a return to a value similar to, but less than the value of the aligned AB structure as the twist angle is reduced to 1.89°. If we extrapolate the trends in C_{44}, and ω_{ZA_2} observed previously [17, 96], the values would continuously decline as the twist angle approached 0°, followed by a sudden large discontinuity as the angle became exactly 0°. At small twist angles $\theta \lesssim 1^\circ$, there are large regions that are close to AA stacking, large regions that are close to AB stacking, and connecting regions that are misaligned. Whether it is appropriate to view the thermal conductivity of such structures as an average of different macroscopic regions of aligned structures and misaligned structures is unclear, but such a view would be consistent with the small-angle trend that we observe. If such a perspective is correct, it raises the question of what length scale determines when such a view is permissible or not.

3.4 Summary, Conclusions, and Open Questions

Large scale room temperature NEMD calculations of the thermal conductivity of twisted bilayer graphene find a non-monotonic dependence of the thermal conductivity on the commensurate lattice constant. At a commensurate lattice constant of 1.1 nm corresponding to an angle of 13.2°, the thermal conductivity falls to 50% of the value of the aligned AB structure. As the commensurate lattice constant increases, the thermal conductivity also increases and reaches 91% of the AB value at a commensurate lattice constant of 7.5 nm corresponding to an angle of 1.89°. The commensurate-lattice-constant-dependent trends in the thermal conductivity are also followed by the trends in the shear elastic constant C_{44}, the wrinkling intensity, and the frequency of the out-of-plane ZA_2 mode. The picture that emerges from these results is that the interlayer misorientation reduces the shear elastic constant C_{44}, the reduced shear elastic constant allows increased wrinkling of the TBG, and the increased wrinkling reduces the thermal conductivity. The small-angle approach of the thermal conductivity towards its value in the aligned structure raises the question of how response functions approach their aligned values as the twist angle approaches 0°. Is the approach gradual, discontinuous, or a combination of the two?

Acknowledgments

This work was supported in part by the National Science Foundation under awards 1307671 and 1433395. Numerical simulations were supported in part by the Spins and Heat in Nanoscale Electronic Systems (SHINES) an Energy Frontier Research Center funded by the U.S. Department of Energy, Office of Science, Basic Energy Sciences under Award #DE-

SC0012670. This work used the Extreme Science and Engineering Discovery Environment (XSEDE) [3] which is supported by National Science Foundation Grant No. ACI-1548562 and allocation ID TG-DMR130081. Used resources include Stampede and Comet.

Appendix

Table. 3.1 shows the calculated elastic constants for each rotation angle along with experimental values and values calculated from DFT. Only C_{44} is affected by misorientation.

Table 3.1: Calculated elastic constants of AB-BLG and TBG. from prior DFT calculation and from our MD calculation using the hybrid REBO and LJ potentials

Rotation angle (°)	C_{11} (GPa)	C_{12} (GPa)	C_{33} (GPa)	C_{44} (GPa)
0(EXP) [97]	1109±16	139±36	38.7±7	5±3
0(DFT) [96]	1109	175	42	4.8
0	1023.6	227.1	42.3	4.79
21.78	1023.6	227.2	42.6	1.65
27.83	1023.8	227.3	42.7	0.411
13.17	1023.3	227.8	42.7	0.293
9.43	1023.7	227.4	42.7	0.503
7.34	1023.7	227.4	42.6	0.618
6.00	1023.6	227.5	42.7	1.485
5.08	1023.8	227.6	42.6	2.47
4.40	1023.5	227.6	42.6	2.53
3.89	1023.2	227.9	42.6	2.57
2.87	1023.5	227.9	42.6	2.89
1.89	1023.4	227.9	42.6	2.90

To verify that the trends shown in Fig. 3.3 are not an artifact of the AIREBO implementation of the LJ potential, we performed a subset of the calculations using REBO+DRIP. Five commensurate angles are selected: 0° (AB), 21.78°, 13.17°, 9.43° and 1.89°. Instead of running multiple simulations of different lengths for each angle and extracting the $L = \infty$ value of the thermal conductivity, we choose one length of $\sim$ 130 nm for each angle and a width of $\sim$ 15 nm. Since the structures are composed of integer numbers of primitive cells that have different sizes, the actual widths lie between 149.12 Å to 150.09 Å, and the lengths range from 1284.88 Å to 1304.14 Å. Due to the finite lengths, the quantitative values will be lower, than those in Fig. 3.3, however, here, we only wish to confirm the non-monotonic trend of the thermal conductivity with the commensurate lattice constant. All other settings related to the NEMD simulations, periodic boundary conditions in the width direction, and temperature (300 K) are as described in the Methods section. It is clear from the results shown in Fig. 3.7 that the trends in the thermal conductivity with respect to the commensurate lattice constant are unaffected by the choice of the interlayer potential.

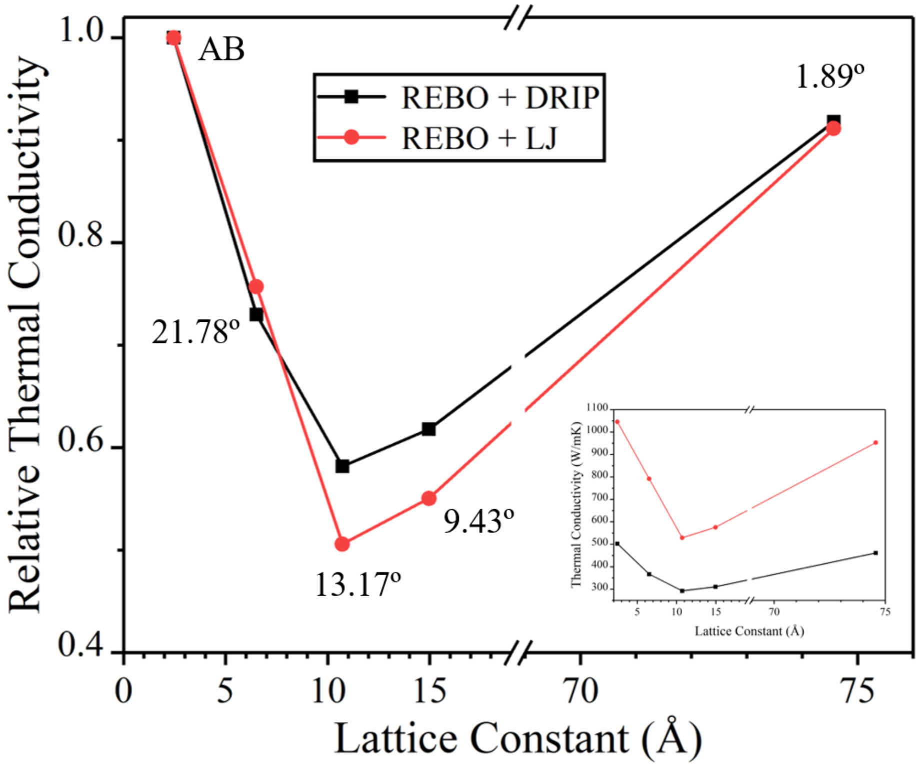

Figure 3.7: Lattice constant dependent relative thermal conductivity (normalized to the AB value) for two different interlayer potentials as shown in the legend. The inset shows the absolute values. The REBO+LJ values are the extracted $L = \infty$ values from Fig. 3.3. The REBO+DRIP values are from the finite length 130 nm structures. Thus, these values are expected to be quantitatively lower.

Chapter 4

Comparative analysis of interatomic potentials for graphene systems

4.1 Introduction

The key to perform an accurate MD simulation is choosing a proper potential for the target system. And unlike SLG, this potential should be suitable for both intralayer and interlayer interactions.

To accurately describe intralayer interactions, a comparison has to be made between the three most widely used potentials of graphene system: Tersoff [84, 85], reactive empirical bond order potential (REBO) [46, 87] and intrinsic long-range bond-order potential for carbon (LCBOP) [88]. Besides LCBOP, other potentials belong to empirical bond order potentials (EBOPs). They are based on the chemical pseudopotential theory created by Abell [89] and treat electronic binding as effective pairs. The influence of local environment around every atom was described by a many-body function and they only consider the interactions between nearest-neighbours. [99] So all EBOPs only have short-range covalent part, which means they need interlayer potentials to describe the long-range Van der Waals (VDW) part, which will be discussed later. Despite the similarities, REBO and Tersoff still have lots of differences. REBO was initially developed as an improved version of Tersoff model. [46] It has different expressions for bond-order, improved angular function at small angles and an extra four-body torsional term. [46, 87] According to the recent semi-empirical potential benchmarks [83, 100] for SLG, REBO beats both Tersoff-1989 [84] and Tersoff-2010 [85] in replicating the lattice constant and phonon dispersion. They evaluate the accuracy by comparing the results with the data collected from density functional theory (DFT) and experiments. The phonon properties of graphene are very sensitive to the structural properties especially the lattice constant, and the thermal conductivity is a function of the acoustic velocity which is directly related to the phonon dispersion. The LCBOP model belongs to the long-range corrected bond-order potential, which by itself has the capability to properly describe the VDW force. [88] It claims that it can better reproduce structural, energetic and elastic properties of single and multilayer graphene compared to EBOPs. [100] According to the benchmarking results, LCBOP does have an overall better performance in phonon dispersion calculations and similar accuracy in structural properties. [83, 100] However, such ascendancy does not guarantee the best performance in thermal conductivity calculation, because the overall better performance of the LCBOP model is due to their high accuracy in reproducing the optical mode. [83] For acoustic modes, on average LCBOP has relatively worse performance than REBO, and its ZA branch has the least accuracy among all of the potentials considered in the benchmark. [83] Another shortcoming of LCBOP is that the dispersion interaction resulting in the VDW force is not considered, even though it is known to be important. This is the primary force governing the ZA mode, so it is not surprising that the ZA mode has the least accuracy with LCBOP.

To accurately describe the interlayer interaction, a comparison between the existing potentials with long rang interactions is necessary. Due to the most widely usage, LJ and LCBOP are considered. Recently, a new type of potential named dihedral-angle-corrected registry-dependent interlayer potential (DRIP) was created to better describe the interlayer VDW forces of multilayer graphene. [90] DRIP is constructed by two parts: one for representing the attractive interaction due to dispersion and another for repulsive interaction due to the anisotropic overlap of electronic orbitals. They claimed that using this potential combined with REBO or Tersoff can reproduce the different stacking energies of multilayer graphene more accurately by the improved repulsive interaction term. [90]

In rest of this section, we will perform potential benchmarking with non-equilibrium molecular dynamics (NEMD) simulations. Both thermal conductivity results and system stability will be considered as the criteria.

4.2 Method

The commensurate angles considered in the benchmarks are 0° (AB-stacking) and 21.78°. The details about how to construct TBG are introduced in the Method section of chapter 3. The NEMD simulations are implemented in the LAMMPS code [45]. The time step is 0.2 fs. There are three steps to the simulation. The relaxation process (step 1) is a constant temperature, 340-ps-long, canonical-ensemble simulation that brings the system temperature up to 300 K as illustrated in Fig. 2.2a. We include a quantum correction [48] to the simulation temperature. The temperature of the BLG increases monotonically to 300 K during the first 150 ps; then the temperature fluctuates around 300 K. At 340 ps, the system reaches a steady temperature of 300 K which indicates that the system is ready to enter the transition process (step 2). The transition process is a 60 ps, constant-energy simulation that ensures that the temperature of the system will maintain an average value of 300 K under a microcanonical ensemble. After the transition process, the system is ready to enter the non-equilibrium process for calculation of the thermal conductivity.

The following interlayer potentials are considered for comparison: LJ, LCBOP. All of them will be combined with intralayer potentials including: Tersoff, REBO and LCBOP. Since LCBOP contains both interlayer and intralayer part, we will not consider the combination of LCBOP with other potentials.

4.3 Results and Discussion

As shown in Table. 4.1, to maintain a stable structure of TBG the choice of intralayer potentials is critical. Although Tersoff has proven to be very successful in predicting phonon properties in SLG, it is not as good as REBO and LCBOP in TBG system due to the layer separation or losing atoms. As the most recent extension originating from the Tersoff potential, REBO maintains a stable TBG structure at room temperature according to the benchmark results. Due to the structural issue, Tersoff will not be considered in our research. Since both LCBOP and REBO+LJ can maintain a stable structure, the thermal conductivity of TBG is calculated using both of them for the final round of comparison. As shown in Table 4.1, using the LCBOP potential, the thermal conductivity difference between AB-BLG and 21.78° TBG is less than 0.5%. While REBO can detect the thermal conductivity reduction ($\sim 25\%$) due to the commensurate rotation, which is consistent with the recent experimental study on the thermal conductivity of TBG by Balandin's group [15]. Due to the best benchmark performance, all calculations will be performed with REBO+LJ.

Table 4.1: Potential benchmark results for TBG by runing NEMD simulations. Unit: W/mK

Interlayer Intralayer	LJ	DRIP	LCBOP
Tersoff-1989	Layer separation in TBG		n/a
Tersoff-1990	Layer separation in TBG		n/a
Tersoff-1994	Lost atoms	Layer separation in TBG	n/a
Tersoff-2005	Layer separation in TBG		n/a
Tersoff-2010	Layer separation in TBG		n/a
LCBOP	n/a		864.13 (AB) 861.22 (21.78°)
REBO	1045.81 (AB) 791.85 (21.78°)	502.78 (AB) 367.06 (21.78°)	n/a

Chapter 5

Low dimensional material data science

There is much current attention on the opportunities afforded by this new field in accelerating materials development and deployment efforts. A particular emphasis is placed on materials exhibiting novel electrical and thermal properties spanning multiple length-/structure scales and the impediments involved in establishing invertible process-structure-property (PSP) linkages for these materials. More specifically, it is argued that modern data sciences (including advanced statistics, dimensionality reduction, and formulation of meta-models) and innovative cyberinfrastructure tools (including integration platforms, databases, and customized tools for enhancement of collaborations among cross-disciplinary team members) are likely to play a critical and pivotal role in addressing the above challenges.

In this chapter, we will describe how to identify the quasi-1D materials from the Material Project Database (MPDB). The structural data from MPDB will be used to predict band gap and identify magnetic materials using machine learning model.

5.1 Dimension classifier

To identify all the quasi-1D materials from MPDB, we created a dimension classifier based on Evan Reed's "find dimension" package [101] implemented in pymatgen module. The fundamental algorithm is shown in Fig. 5.1. The part inside the dashed red box is the adding method to identify quasi-1D materials from 2D materials. The default criteria for the "find cluster" method is 0.5 Å, while the reduced criteria is 0.2 Å. The dimension classifier code along with the manual is attached Appendix A.2.

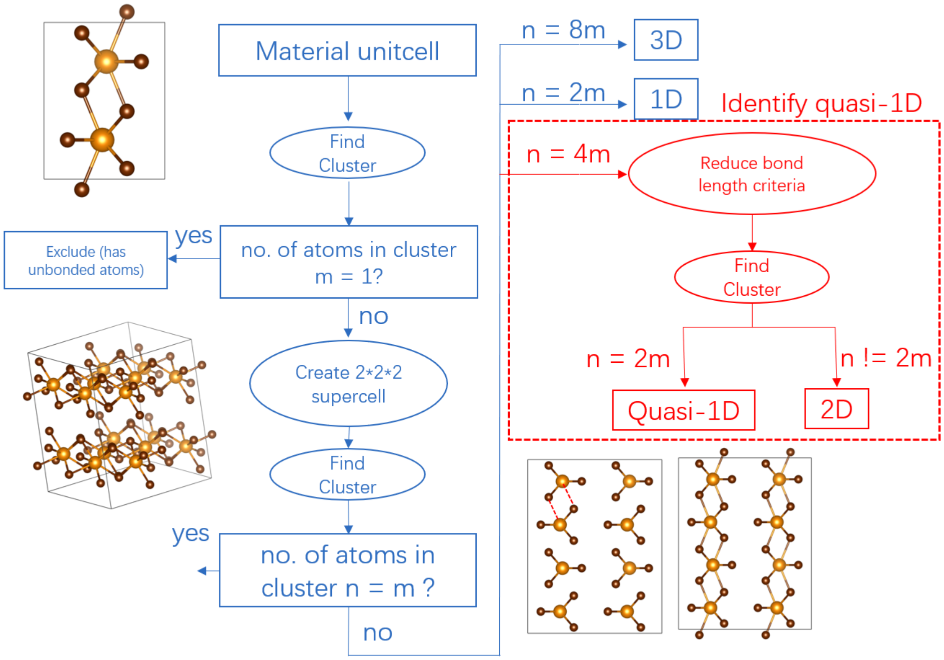

Figure 5.1: Algorithm to classify the dimension of given material. Input: material unitcell with .cif format. Output: dimensions (0D, 1D, quasi-1D, 2D, 3D, intercalated ion and intercalated molecule).

Using this code, the identified quasi-1D materials sorted by the band gap and total magnetization are shown in Table 5.1 and Table 5.2, respectively. And we also attached the identified 1D materials sorted by the total magnetization in Table 5.3. The data will be useful for the theoretical and experimental study.

Table 5.1: quasi-1D materials identified from MPDB sorted by the band gap.

MPID	**Material Formula**	**Band Gap (eV)**
mp-558387	TeOF2	4.189
mp-753858	TiOF2	3.8984
mp-28448	DyCl3	3.8951
mp-23293	TbCl3	3.798
mp-753800	NbOF3	3.6661
mp-31320	Nd(C2N3)3	3.5983
mp-567763	Pr(C2N3)3	3.5811
mp-31321	La(C2N3)3	3.5567
mp-29185	Te2O3F2	3.3405
mp-561533	SbOF	3.3231
mp-27976	SmBr3	2.9285
mp-27975	NdBr3	2.9222
mp-28580	Y2NCl3	2.1398
mp-28299	USe2O7	2.1387
mp-680334	LaSb(SBr)2	2.0983
mp-27725	AuI	2.0853
mp-27979	LaI3	2.0652

Continued on next page

Table 5.1 – continued from previous page

MPID	Material Formula	Band Gap (eV)
mp-27697	ThI4	1.8297
mp-9481	TcS2	1.1449
mp-9922	HfS3	1.1188
mp-9921	ZrS3	1.0991
mp-705486	U3Cu2H10(CO10)2	0.7648
mp-28375	Ta2AgF12	0.7135
mp-638749	Te3(PdBr)4	0.6621
mp-567478	MnSbSe2Br	0.6263
mp-14653	AgSb2F12	0.5352
mp-570268	MnSbSe2I	0.5335
mp-573321	TePdI2	0.5268
mp-556582	Cu(IO3)2	0.4893
mp-1683	ZrSe3	0.4382
mp-13542	ZrGeTe4	0.4017
mp-28965	AgBi2F12	0.3605
mp-562100	NbS3	0.3568
mp-567817	HfGeTe4	0.3467

Continued on next page

Table 5.1 – continued from previous page

MPID	Material Formula	Band Gap (eV)
mp-15622	HfSe3	0.308
mp-649601	RuXeF11	0.3055
mp-28571	La2Br5	0.2976
mp-570506	ZrI2	0.2939
mp-23169	Pr2Br5	0.2826
mp-9920	TiS3	0.2318
mp-30282	La2I5	0.1781
mp-22854	Pr2I5	0.1295
mp-684706	LaO3	0.0223
mp-17588	AgRuF7	0
mp-581990	Bi3Rh	0
mp-567687	CrI2	0
mp-753975	Dy2(BiO2)7	0
mp-680500	PtXeF11	0
mp-28308	Ta2NiS5	0
mp-541183	Ta2NiSe7	0
mp-8435	Ta2PdS6	0

Continued on next page

Table 5.1 – continued from previous page

MPID	Material Formula	Band Gap (eV)
mp-8436	Ta2PdSe6	0
mp-14474	Ta2PtSe7	0
mp-30527	TaS3	0
mp-29652	TaSe3	0
mp-8357	UTe3	0
mp-2089	ZrTe3	0

Table 5.2: quasi-1D materials identified from MPDB sorted by the total magnetization.

MPID	Material Formula	Total Magnetization (A/m)
mp-567478	MnSbSe2Br	5.000002725
mp-570268	MnSbSe2I	5.00000005
mp-567687	CrI2	4.000114
mp-17588	AgRuF7	2.999999875
mp-649601	RuXeF11	2.95321195
mp-8357	UTe3	2
mp-705486	U3Cu2H10(CO10)2	1.9999071
mp-22854	Pr2I5	1.0006243

Continued on next page

Table 5.2 – continued from previous page

MPID	Material Formula	Total Magnetization (A/m)
mp-23169	Pr2Br5	1.00037625
mp-28571	La2Br5	1.0002548
mp-28965	AgBi2F12	1.0000001
mp-14653	AgSb2F12	1
mp-30282	La2I5	1
mp-28375	Ta2AgF12	0.9999999
mp-556582	Cu(IO3)2	0.9999998
mp-684706	LaO3	0.99579195
mp-680500	PtXeF11	0.9278836
mp-14474	Ta2PtSe7	0.02779195
mp-638749	Te3(PdBr)4	0.00010445
mp-581990	Bi3Rh	0.0000144
mp-753975	Dy2(BiO2)7	0.0000111
mp-570506	ZrI2	0.000007375
mp-28448	DyCl3	0.00000575
mp-8435	Ta2PdS6	0.0000022
mp-541183	Ta2NiSe7	0.0000018

Continued on next page

Table 5.2 – continued from previous page

MPID	Material Formula	Total Magnetization (A/m)
mp-680334	LaSb(SBr)2	0.000001525
mp-8436	Ta2PdSe6	0.0000004
mp-23293	TbCl3	0.00000035
mp-13542	ZrGeTe4	0.00000015
mp-15622	HfSe3	0.00000005
mp-558387	TeOF2	0
mp-753858	TiOF2	0
mp-753800	NbOF3	0
mp-31320	Nd(C2N3)3	0
mp-567763	Pr(C2N3)3	0
mp-31321	La(C2N3)3	0
mp-29185	Te2O3F2	0
mp-561533	SbOF	0
mp-27976	SmBr3	0
mp-27975	NdBr3	0
mp-28580	Y2NCl3	0
mp-28299	USe2O7	0

Continued on next page

Table 5.2 – continued from previous page

MPID	Material Formula	Total Magnetization (A/m)
mp-27725	AuI	0
mp-27979	LaI3	0
mp-27697	ThI4	0
mp-9481	TcS2	0
mp-9922	HfS3	0
mp-9921	ZrS3	0
mp-573321	TePdI2	0
mp-1683	ZrSe3	0
mp-562100	NbS3	0
mp-567817	HfGeTe4	0
mp-9920	TiS3	0
mp-28308	Ta2NiS5	0
mp-30527	TaS3	0
mp-29652	TaSe3	0
mp-2089	ZrTe3	0

Table 5.3: 1D materials identified from MPDB sorted by the total magnetization.

MPID	Material Formula	Band Gap (eV)	Total Magnetization (A/m)
mp-735662	Fe4As10PbO22	1.7469	19.99812645
mp-541385	Cs6Fe2O5	1.5098	7.996752
mp-765941	Mn2F7	1.8053	7.00110275
mp-867369	TcF3	0.1714	6.0281908
mp-676241	FeCl3	0.8119	5.00768555
mp-25540	MnH4(CO3)2	2.3683	5.0017518
mp-566645	MnH6SO6	4.4475	5.00110965
mp-28912	MnInBr3	1.6239	5.0007345
mp-683891	MnSb6(Pb2S7)2	0.447	5.00065735
mp-771047	Mn(IO3)2	2.5127	5.0004147
mp-25770	MnH6(SO4)4	5.0995	5.00031185
mp-540676	MnH4(ClO)2	4.3746	4.9999998
mp-10412	Mn(SbS2)2	0	4.99984055
mp-638590	MnTl2GeTe4	0.1865	4.9997786
mp-566172	MnH10S2(NO2)4	4.3533	4.9992838
mp-553927	Pu(IO3)4	0.091	4.03017185
mp-504883	FeH4(ClO)2	4.1399	4.0080385

Continued on next page

Table 5.3 – continued from previous page

MPID	**Material Formula**	**Band Gap(eV)**	**Total Magnetization (A/m)**
mp-772432	FeH4(SO5)2	0.0724	4.0007409
mp-22369	FeSb6(Pb2S7)2	0	4.0000343
mp-743926	FeH4(CO3)2	2.5092	4.0000203
mp-22857	CrCl2	0.7019	4.000005
mp-27215	CrI2	0.0153	3.9999999
mp-763306	CrH10S2(NO2)4	2.9651	3.9999995
mp-744256	MnH5SO7	0.6941	3.999406775
mp-540759	Al2CoCl8	0.3251	3.00077565
mp-772662	MnH4(SO5)2	0.6868	3.0004849
mp-629319	CoSb2S2(OF3)4	2.9027	3.0004673
mp-765253	MnF4	0.7666	3.00028125
mp-15236	CrSbSe3	0.4753	3.00019625
mp-9130	CrSbS3	0.5818	3.000113375
mp-774233	Co(IO3)2	2.3533	3.000053825
mp-743783	CoP4(H5O8)2	3.2039	2.9999996
mp-23244	UI3	0.0954	2.9999898
mp-25492	CoH4(CO3)2	2.4737	2.9998627

Continued on next page

Table 5.3 – continued from previous page

MPID	Material Formula	Band Gap(eV)	Total Magnetization (A/m)
mp-568443	Al2VCl8	1.6263	2.99964085
mp-570480	TcBr4	0.6025	2.998397363
mp-27780	TcCl4	0.7829	2.994713325
mp-555999	Np(IO3)4	0.2239	2.99109995
mp-778446	Cr2(PS4)3	0	2.926512225
mp-864733	MoI3	0	2.65673565
mp-28301	OsBr4	0	2.0203318
mp-542131	UTe4Br5	0.0029	2.0033179
mp-605912	Al2NiCl8	1.1343	2.00150305
mp-684560	MoCl4	0	2.00137
mp-558794	Cu2BH5O6	0.0409	2.001127275
mp-695793	ZnAs4(HO2)8	0.1253	2.0005229
mp-765097	W2OF8	2.5313	2.00042885
mp-653062	Mo2Cl8O	0.9227	2.000096275
mp-558341	CrXeF6	1.7998	2.000000025
mp-23312	MoBr3	0.6926	1.999946325
mp-704123	CrF4	1.5634	1.99989625

Continued on next page

Table 5.3 – continued from previous page

MPID	Material Formula	Band Gap(eV)	Total Magnetization (A/m)
mp-571035	OsCl4	0.5105	1.9998556
mp-865473	VBr3	0	1.99977245
mp-566902	Te3W2Se4(Cl4O)2	1.0027	1.9996633
mp-772376	Ni(IO3)2	2.8257	1.99959755
mp-655360	UI4	0.2676	1.9992569
mp-865493	VI3	0	1.9992233
mp-866812	UTa2S6Cl6O	0.183	1.99070055
mp-862851	PaI3	0	1.98446405
mp-570722	NbI3	0	1.3745771
mp-28321	Sc7CI12	0	1.1592062
mp-542135	Mo2NCl7	0.0046	1.07044505
mp-541102	Sc6C2I11	0.0154	1.0380839
mp-680309	Mo2NCl8	0	1.00786695
mp-504921	Sc7CBr12	0.1005	1.006156
mp-606617	CuSb2(XeF8)2	0.0694	1.0057132
mp-774723	CuH12C3SN6O7	0.5787	1.0028137
mp-703531	CuSiH8(O2F3)2	0.9868	1.00124025

Continued on next page

Table 5.3 – continued from previous page

MPID	Material Formula	Band Gap(eV)	Total Magnetization (A/m)
mp-622116	ReOF4	0.9318	1.001086713
mp-720299	ZrCuH8(O2F3)2	0.8695	1.0010209
mp-764115	V3O7	1.1608	1.000820067
mp-639662	CrF5	1.3584	1.000487225
mp-24362	CuH6CN2O3	0.5795	1.000117025
mp-707170	CuH6SO7	0.7765	1.00010565
mp-566402	CrSbF10	1.31	1.000083175
mp-25062	MoCl3O	2.4587	1.00008085
mp-765216	VF4	1.5907	1.000067738
mp-632759	CuH4(OF)2	0.2541	1.0000034
mp-19243	VSb2O5	2.5772	1.00000055
mp-765500	V2OF7	2.4201	1.0000001
mp-565978	WCl3O	1.719	1.000000025
mp-1852	UF5	0.7489	0.9999999
mp-643913	CoH6(NCl)2	0.2352	0.9999953
mp-30999	CuCl2	0.0333	0.9998947
mp-570568	W2NCl8	0.1574	0.9998106

Continued on next page

Table 5.3 – continued from previous page

MPID	**Material Formula**	**Band Gap(eV)**	**Total Magnetization (A/m)**
mp-696152	CuSnH12(NO3)2	0.8126	0.9992447
mp-680300	Mo3N2Cl11	0.1598	0.986204
mp-567624	CrBr2	0	0.5777743
mp-27340	ReCl4	0	0.483597975
mp-556538	Na8(CuO2)5	0	0.4526595
mp-16977	Ti(MnP6)2	0.0012	0.4512632
mp-571143	TiCl3	0	0.25085525
mp-27978	PuI3	0	0.2131271
mp-504781	NpI3	0.0004	0.09440445
mp-541826	Ti(AlBr4)2	0	0.09194745
mp-685385	Tl2In3Se5	0.6106	0.0594165
mp-23294	RuBr3	0	0.02999935
mp-864915	HfBr3	0	0.0260708
mp-675519	Tl3In7Se10	0.5683	0.02089365
mp-541175	Sc7CoI12	0.2411	0.0176131
mp-862773	TeI2	0.7144	0.01691595
mp-23219	CuBr2	0	0.0108531

Continued on next page

Table 5.3 – continued from previous page

MPID	Material Formula	Band Gap(eV)	Total Magnetization (A/m)
mp-29279	CuClF10	0.0247	0.01069785
mp-683982	RuOF4	0.298	0.007980838
mp-559817	Na3(CuO2)2	0	0.006828375
mp-674324	Sn7(SBr5)2	2.014	0.0059585
mp-556436	Sb2BrF15	2.8579	0.00528455
mp-541032	Te7As5I	0.3024	0.0047946
mp-621960	Sb4Pb4S11	0	0.00393345
mp-29178	TePbF6	4.6008	0.003859625
mp-654051	Nb6SI9	0	0.0032187
mp-865005	DyI3	2.1725	0.00321095
mp-655489	Pb4SeBr6	1.9565	0.0029662
mp-770274	NiP4	0	0.002874525
mp-561241	USb3O2F17	2.4478	0.0028572
mp-758096	SbOF3	1.9231	0.00256145
mp-27199	AuSeBr	0.6295	0.002385625
mp-766269	ZnPH5C2N4O3	4.5292	0.002346725
mp-697033	CdH4CN2Cl2O	3.5746	0.00232125

Continued on next page

Table 5.3 – continued from previous page

MPID	Material Formula	Band Gap(eV)	Total Magnetization (A/m)
mp-758957	As2HPbF13	4.5547	0.002317838
mp-759848	Bi4O5F2	2.4866	0.002275475
mp-864657	HoI3	2.2173	0.0021535
mp-567661	MoPCl5O3	2.3144	0.002078713
mp-556117	Ga3Pb5F19	4.7168	0.0017115
mp-703352	UP2H6O7	2.5385	0.001556825
mp-866214	LuBr3	3.0669	0.00150055
mp-540925	Hg2AsF6	0.7379	0.0014388
mp-555059	TcSb(OF4)2	2.8188	0.00143285
mp-571465	PbIBr	2.5643	0.001391225
mp-484	Te3As2	0.4367	0.00132105
mp-20326	U(PS3)2	0	0.00131045
mp-31268	AlBiBr6	2.5681	0.00130635
mp-29862	SnBr2	2.5388	0.00127605
mp-605347	HgTe(H2O3)2	2.0783	0.001236575
mp-24053	AgH2ClO5	2.8242	0.001230275
mp-541155	VS4	0.9396	0.001226025

Continued on next page

Table 5.3 – continued from previous page

MPID	Material Formula	Band Gap(eV)	Total Magnetization (A/m)
mp-567264	SbMoOF9	3.6798	0.0012058
mp-733848	CdRe2H8C2(N2O5)2	2.7675	0.001175025
mp-864982	DyBr3	3.0029	0.00117225
mp-24714	ZnH4(CO3)2	3.1831	0.001161
mp-625272	Zn(HO)2	2.0603	0.0011546
mp-24307	CdH8C4(S2N3)2	3.2788	0.0011517
mp-669496	PtI4	0.6934	0.001144475
mp-569175	ZrCl4	3.6105	0.0011
mp-31487	NbI5	0.5983	0.00109525
mp-558199	CuAs4S3Cl	1.6217	0.001056925
mp-649616	Pd(XeF8)2	1.4046	0.001046025
mp-27907	Sb6Pb4S13	0.8506	0.0009705
mp-554819	MgP4(Cl5O3)2	3.5985	0.0009573
mp-557926	CdAs2(XeF5)4	2.3694	0.0009497
mp-570857	Y(AlCl4)3	4.0292	0.000948433
mp-861867	AcI3	2.5886	0.00093485
mp-568896	La(AlBr4)3	2.6083	0.0009292

Continued on next page

Table 5.3 – continued from previous page

MPID	**Material Formula**	**Band Gap(eV)**	**Total Magnetization (A/m)**
mp-570880	RuCl3	0	0.000909
mp-555121	MgAs2S2(OF3)4	3.5807	0.000902625
mp-556434	AgBi(PS3)2	1.1797	0.0008917
mp-753246	Sn3(OF)2	0	0.000887125
mp-560633	Al2SnCl6O	3.959	0.000876975
mp-29796	Ho(AlCl4)3	4.31	0.000853833
mp-567874	Pr(AlBr4)3	3.3654	0.0008395
mp-765597	HS2IO8	2.7665	0.00083895
mp-28757	Nd(AlBr4)3	3.3848	0.000836933
mp-17867	Mn2NbP12	0	0.0008255
mp-865301	TmBr3	2.9866	0.00082165
mp-768283	UAs2H6O11	2.3704	0.00081335
mp-743614	MoH2Cl2O3	2.6258	0.0008109
mp-560464	UTl2(TeO4)2	1.8322	0.000784525
mp-640341	Mo3S7Cl4	1.6678	0.00078275
mp-21653	BaNiN	0	0.000781442
mp-570417	Bi6PtCl10	1.5756	0.000747438

Continued on next page

Table 5.3 – continued from previous page

MPID	Material Formula	Band Gap(eV)	Total Magnetization (A/m)
mp-567318	TlSbSe2	0.6743	0.0007387
mp-23493	Ce(IO3)4	1.4876	0.00073345
mp-619661	Pb3(IO)2	2.2335	0.000732575
mp-27317	SbAsF8	3.8632	0.00072175
mp-606393	NbBr3O	1.9611	0.000704525
mp-558330	IClOF	2.0229	0.0006892
mp-865605	YBr3	2.9454	0.0006646
mp-540924	NbTeI3	0.4539	0.00065345
mp-23536	SbI3Cl8	1.1884	0.0006528
mp-759602	Sb4O5F2	2.8185	0.0006504
mp-705569	NiB18(H11C2)2	1.5217	0.000647425
mp-864662	HoCl3	3.7011	0.00064075
mp-27742	K2CdO2	1.3576	0.000623475
mp-24294	HgHClO4	2.3817	0.000619175
mp-28509	Ta4SiTe4	0.0286	0.000608475
mp-632706	ZnH8(N2Cl)2	4.5084	0.0006004
mp-680836	Ta4Te9I4O	0.3812	0.0005985

Continued on next page

Table 5.3 – continued from previous page

MPID	Material Formula	Band Gap(eV)	Total Magnetization (A/m)
mp-862986	PmBr3	2.8814	0.00058955
mp-24337	MgH2Cl2O	5.3707	0.00058835
mp-29946	IO2F	2.8952	0.00058695
mp-541772	Bi4RuBr2	0.5304	0.00058485
mp-24460	MgH6(SO4)4	5.9617	0.0005843
mp-759866	TeH3CCl3	2.9222	0.0005738
mp-643387	AlH2PbO2F3	4.4942	0.0005621
mp-505284	Pb3(BrO)2	2.3882	0.000557475
mp-28135	NbXeF11	2.648	0.000536475
mp-583499	Bi6PtBr10	1.4291	0.0005361
mp-541094	Ta2Hg3S(O2F5)2	2.4414	0.00052705
mp-3785	TlGaTe2	0.5317	0.00052505
mp-648414	V2PS10	1.1097	0.000523763
mp-757173	Sb5O7F	3.078	0.0005105
mp-754661	INO3	1.6497	0.00050095
mp-610491	BiSeCl	1.8404	0.000498825
mp-570951	Ti(AlCl4)2	0.0552	0.0004911

Continued on next page

Table 5.3 – continued from previous page

MPID	Material Formula	Band Gap(eV)	Total Magnetization (A/m)
mp-28256	V2Se9	0.713	0.00047305
mp-865324	LuCl3	3.8453	0.00046535
mp-23408	Tl4Bi2S5	0.9897	0.000453875
mp-645740	SnSO4	3.5219	0.0004498
mp-865353	TmI3	2.2545	0.0004484
mp-29469	Pd(Se3Cl)2	1.28	0.00044555
mp-27628	Te3Cl2	1.3482	0.00044275
mp-865521	LuI3	2.1804	0.0004401
mp-780501	CrB3(HO3)3	2.1189	0.000432625
mp-764274	VOF3	3.4012	0.0004296
mp-566001	CrHg(PbO3)2	2.0835	0.0004235
mp-541106	Nb2Se9	0.7637	0.0004194
mp-31040	NbCl4	1.0765	0.00041665
mp-703539	AgB11H6CBr6	3.2973	0.000414425
mp-30938	PAuS4	1.3165	0.00041045
mp-30150	GaBH6	4.8941	0.000403083
mp-758899	Sb2OF8	2.1564	0.00039585

Continued on next page

Table 5.3 – continued from previous page

MPID	Material Formula	Band Gap(eV)	Total Magnetization (A/m)
mp-626865	H2WO5	2.4402	0.00037915
mp-22856	Bi2S3	1.3618	0.00037645
mp-9579	AlTlSe2	0.5873	0.00037515
mp-14249	Th(PS3)2	2.4371	0.0003656
mp-28149	Bi9I2	0	0.0003624
mp-603254	PH9AuC3S3Cl	2.8803	0.000354888
mp-753785	NbOF3	3.2629	0.000348325
mp-768093	VSO4F3	0.9283	0.000344675
mp-752422	IClO	1.0256	0.00034275
mp-29483	MgInBr3	2.0567	0.000336125
mp-570553	FeP4	0.8043	0.000326675
mp-864617	NdI3	2.0128	0.00032095
mp-29526	BrNO3	2.1636	0.00031745
mp-760758	Bi3O4F	2.1905	0.0003172
mp-745159	MoPH3O7	3.1857	0.00031165
mp-29422	HfCl4	4.1644	0.0003111
mp-556130	GeXeF10	2.3433	0.000308725

Continued on next page

Table 5.3 – continued from previous page

MPID	Material Formula	Band Gap(eV)	Total Magnetization (A/m)
mp-571061	Nb3Se10Cl3	1.093	0.0002921
mp-754005	Mg(CO2)2	3.4504	0.0002838
mp-541013	TiI4	1.0867	0.00028305
mp-541610	GeBr2	2.597	0.00027495
mp-29573	Sb4S5Cl2	1.8692	0.00026945
mp-29465	TaCl4	1.2222	0.0002603
mp-758829	Nb2OF8	4.2124	0.0002593
mp-27436	PaCl5	2.4189	0.0002472
mp-541732	Al3Pb5F19	5.1376	0.00024505
mp-29190	Te4MoBr	0.855	0.00024185
mp-556425	SbF4	3.4408	0.0002347
mp-567484	PtCl2	1.1359	0.0002326
mp-504575	MoOF4	4.1739	0.000228938
mp-9580	TlGaSe2	0.561	0.00022875
mp-543028	Tl2TeO3	1.9408	0.000227763
mp-29018	ZrSnCl6	2.2258	0.000224717
mp-769377	SbSO4F3	1.8163	0.00022025

Continued on next page

Table 5.3 – continued from previous page

MPID	**Material Formula**	**Band Gap(eV)**	**Total Magnetization (A/m)**
mp-862983	InCl3	3.0122	0.0002184
mp-24215	ScH3Br3N	3.1435	0.000214625
mp-27684	Tl4O3	1.0973	0.0002113
mp-580999	Ga2NiCl8	0.5238	0.0002086
mp-676362	HIO4	1.5685	0.000207175
mp-558408	Nb4Te9I4O	0.2533	0.00020445
mp-554764	Sb3Au3F22	0.0795	0.0002038
mp-4649	PdSe2O5	0.9947	0.00020325
mp-27655	Te2I	0.6558	0.00020275
mp-8251	VP4	0	0.0002019
mp-27373	SnClF	3.4438	0.00020055
mp-27866	MoS2Cl3	1.4364	0.00020015
mp-30937	HgClO3	3.0661	0.000194563
mp-541093	Nb2Hg3S(O2F5)2	2.3509	0.00019205
mp-1509	Sn2S3	0.7755	0.000188625
mp-24509	CdH4(BrO4)2	3.9715	0.00018655
mp-28038	NbTeBr3	0.5913	0.000179775

Continued on next page

Table 5.3 – continued from previous page

MPID	Material Formula	Band Gap(eV)	Total Magnetization (A/m)
mp-625112	H8PtO6	1.5662	0.0001795
mp-28005	As2(SO4)3	4.5714	0.000179325
mp-769355	AgH3O2	1.0711	0.000178738
mp-19941	As2PbS4	0.765	0.00017765
mp-22871	ZrCl3	0	0.00017605
mp-29492	S2I2O11	2.6242	0.000170925
mp-30159	AuBrF6	1.9127	0.00017085
mp-561299	As2Pb4S6ICl	1.829	0.00016895
mp-28885	PSe	2.2421	0.000168006
mp-768315	Mg(IO3)2	3.3254	0.000167575
mp-569766	TeI	0.7163	0.000165425
mp-23041	SbSI	1.6354	0.000164875
mp-570140	AuBr	1.9716	0.00015345
mp-778385	B3H3SeO9	3.2394	0.000150738
mp-569522	MnP4	0.4803	0.00014855
mp-867875	SmCl3	3.4912	0.00014835
mp-28683	Ta(ICl)2	1.1785	0.00014585

Continued on next page

Table 5.3 – continued from previous page

MPID	Material Formula	Band Gap(eV)	Total Magnetization (A/m)
mp-641112	ReO2F3	3.2953	0.000144588
mp-540540	PaBr3O	1.7543	0.0001401
mp-23355	PAuCl4	2.5498	0.000139575
mp-23498	NbSeBr3	0.7309	0.00013715
mp-568146	Pd(Se3Br)2	1.0268	0.0001361
mp-510421	CrO3	2.2551	0.0001352
mp-754514	N2	0	0.0001324
mp-29844	Tb(AlCl4)3	4.2153	0.000125067
mp-861871	SeI2	0.8854	0.0001207
mp-540615	Nb3Se5Cl7	0.9467	0.00011995
mp-556422	NbCl3O	2.8024	0.000119425
mp-27648	Te2Br	0.6563	0.00011835
mp-567998	ICl	1.8269	0.0001154
mp-8725	HfSnS3	1.1982	0.000113575
mp-505373	AsSeI	1.242	0.000110825
mp-28460	Br2O	1.3644	0.000104075
mp-541037	CsCuO	1.1227	0.00010305

Continued on next page

Table 5.3 – continued from previous page

MPID	**Material Formula**	**Band Gap(eV)**	**Total Magnetization (A/m)**
mp-32479	Tl3VO4	2.5951	0.0001027
mp-557163	TaPbF7	5.1278	0.00010245
mp-505357	InSeI	1.4358	0.000101425
mp-20244	ZrPbS3	1.2455	0.000100275
mp-569152	SnCl2	3.0724	0.000098875
mp-22600	Sc3P2	0	0.000098725
mp-572597	SbPS4	2.0791	0.0000984
mp-2160	Sb2Se3	0.7564	0.000096175
mp-643902	SnH4(NF)2	3.1067	0.0000958
mp-23963	HIO3	3.213	0.0000946
mp-23247	ZrBr3	0	0.0000946
mp-28364	Rb2CdO2	1.3087	0.0000932
mp-2809	Sb2S3	1.2828	0.0000907
mp-22232	TlInSe2	0.7351	0.00008855
mp-684021	Sn4Sb6S13	0.6014	0.0000874
mp-8759	Cs2ZrO3	3.854	0.00008545
mp-23291	PbCl2	3.7939	0.0000848

Continued on next page

Table 5.3 – continued from previous page

MPID	Material Formula	Band Gap(eV)	Total Magnetization (A/m)
mp-569017	PdI2	0.8733	0.00008475
mp-554724	CuP4S3I	1.7032	0.000082775
mp-571235	ZrI4	2.0134	7.98833E-05
mp-753806	BSbO3	3.762	0.00007975
mp-28693	Al3Te3I	1.9651	0.000079125
mp-541771	Bi4RuI2	0.4519	0.0000791
mp-13923	SnPS3	2.1282	0.000078075
mp-504564	Si(PbS2)2	2.0437	0.0000753
mp-764232	VO2F	3.0505	0.000074225
mp-757256	ZnH4(IO4)2	3.2826	0.000073
mp-770164	V2SO8	1.8925	0.000072925
mp-556078	MgAs2(XeF8)2	2.9713	0.00007215
mp-753233	Sb6O5F8	3.3506	0.0000721
mp-568002	HfI3	0	0.00007175
mp-626577	Mo(HO2)2	3.1832	0.00006795
mp-768223	Cs2CeO3	2.2437	0.000066
mp-541785	GePdS3	1.3072	0.0000651

Continued on next page

Table 5.3 – continued from previous page

MPID	Material Formula	Band Gap(eV)	Total Magnetization (A/m)
mp-561397	SO3	5.1414	0.000064775
mp-23170	IO2	1.4525	6.36625E-05
mp-546285	NbI3O	0.8108	0.00005685
mp-637982	As5Pb3S10	0.488	0.000056075
mp-28974	TiF4	4.166	5.53167E-05
mp-28661	Ba2Cu3P4	0	0.0000551
mp-567731	Nb3Se10Br3	1.2229	0.00005465
mp-571146	SnICl	2.5132	0.00005455
mp-570270	NbSeCl3	0.7501	0.00005265
mp-571555	InCl	2.1996	0.00005205
mp-29251	Te6Br2O11	2.5231	0.00005135
mp-686102	Tl3In2Se5	0.6144	5.01375E-05
mp-322	TlS	0.7034	0.000048725
mp-861891	SeBr2	0.8221	0.00004835
mp-569059	HfI4	2.3528	0.000046425
mp-638022	Sb4Pb5S11	1.3758	0.000044
mp-24741	ScH3NCl3	3.8496	0.00004385

Continued on next page

Table 5.3 – continued from previous page

MPID	Material Formula	Band Gap(eV)	Total Magnetization (A/m)
mp-20408	InGaTe2	0	0.00004355
mp-756372	Rb2MgO2	2.2799	0.00004185
mp-504814	Sb2Pb2S5	1.0418	0.000041275
mp-558797	VF5	2.9917	0.00004005
mp-22147	HfPbS3	1.452	0.000039625
mp-22870	InBr	1.2575	0.00003955
mp-634812	H2O	5.3268	0.000039375
mp-7609	SbOF	3.3084	0.00003905
mp-27639	IBr	1.4023	0.00003825
mp-573051	ReO3F	3.0005	3.75833E-05
mp-8781	SnS	1.8201	0.000037
mp-28857	Pb(IO3)2	2.6939	0.000036475
mp-27857	PdBr2	0.8979	3.53625E-05
mp-21365	InSbS3	1.4761	0.0000348
mp-28714	Dy(AlCl4)3	4.2606	3.47333E-05
mp-28845	OsO3F2	2.3101	0.000034725
mp-22997	PbBrCl	3.4376	0.00003465

Continued on next page

Table 5.3 – continued from previous page

MPID	Material Formula	Band Gap(eV)	Total Magnetization (A/m)
mp-22971	SbSBr	1.7648	0.00003435
mp-27735	GaSbCl6	3.928	0.00003375
mp-12027	TaTlSe3	0.3102	0.0000305
mp-28608	Ga3Te3I	1.2591	0.00002985
mp-608653	As2Pb2S5	1.6038	2.90625E-05
mp-29579	Sc7NCl12	0.0043	0.0000271
mp-560625	RePbClO4	3.3739	0.0000264
mp-23297	BrF3	2.1576	0.0000248
mp-726	SeO2	3.2709	2.46625E-05
mp-541593	ZrPb2F8	5.2222	0.000023375
mp-680181	Bi2Pb2S5	0.7228	2.32375E-05
mp-757220	LuH6(ClO5)3	5.3849	0.0000225
mp-570188	ZrI3	0.0747	0.000020325
mp-623984	PbSO4	3.8567	0.000020175
mp-2511	PbF2	4.3823	0.000019075
mp-23407	Hg(IO3)2	2.6917	0.0000187
mp-23202	InI	1.3414	0.0000181

Continued on next page

Table 5.3 – continued from previous page

MPID	Material Formula	Band Gap(eV)	Total Magnetization (A/m)
mp-21904	PbS2O3	3.5394	0.0000168
mp-3245	SnP7Au3	0.0281	0.00001505
mp-20320	InTe	0	0.000014425
mp-22747	Pb(CO2)2	2.7868	0.0000131
mp-756448	LaMgI5	1.9817	0.000013
mp-23264	TiI3	0.1604	0.000012275
mp-554896	SbXe2OF15	1.2419	0.00001225
mp-765135	WOF4	4.4088	0.0000113
mp-28077	PbBr2	3.1375	0.0000106
mp-561664	TeF4	4.0186	0.00001035
mp-29500	Ge7F16	4.3804	0.0000095
mp-27308	SbBrF8	2.6902	0.000008625
mp-28964	Ta4FeTe4	0	0.000008
mp-634	HgS	1.7068	0.0000074
mp-569008	PdCl2	0.9097	0.000007
mp-866003	ErI3	2.0376	0.0000067
mp-561449	OsOF4	0.6713	0.0000063

Continued on next page

Table 5.3 – continued from previous page

MPID	Material Formula	Band Gap(eV)	Total Magnetization (A/m)
mp-20526	PbS	2.0909	0.000006
mp-9847	YbP5	0	0.0000055
mp-28804	TcO2F3	2.5259	0.0000042
mp-17324	ZrSnS3	0.995	0.00000355
mp-27472	NbSbF10	4.3499	0.0000032
mp-20507	PbSO3	3.6372	0.0000029
mp-8203	Zr(PS3)2	1.5319	0.0000027
mp-20716	PbSeO3	2.8838	0.0000024
mp-542694	HI3O8	2.5131	0.000002075
mp-27133	BiPS4	1.4839	1.9375E-06
mp-27358	Se2O5	2.885	0.0000017
mp-27462	AlPS4	2.6141	0.00000155
mp-862800	PrI3	1.9521	0.0000015
mp-15046	Sb2(PSe3)3	1.4601	0.000001325
mp-7302	CrP4	0	0.0000013
mp-572284	SbXeOF9	2.2	0.0000012
mp-28954	Tl2PdSe2	0	0.000001

Continued on next page

Table 5.3 – continued from previous page

MPID	Material Formula	Band Gap(eV)	Total Magnetization (A/m)
mp-27994	HgBrO3	3.1922	0.000000875
mp-27743	BiF5	1.8138	0.0000008
mp-863658	PmCl3	3.5399	0.0000007
mp-542769	Sn(CO2)2	2.6084	0.0000006
mp-557705	OsO2F3	0.5722	0.000000575
mp-573815	ReI3	0.947	5.33333E-07
mp-863695	PmI3	2.0675	0.0000005
mp-583234	Bi4I	0	0.000000475
mp-570044	NbI4	0.478	0.0000004
mp-568100	ReNCl4	1.0777	0.0000004
mp-28051	SbTeI	0.8606	0.0000004
mp-568758	BiBr	1.0369	3.375E-07
mp-540639	FeH8C4(S2N3)2	0.5768	0.0000003
mp-733929	P2H4PbO8	4.4499	0.0000003
mp-753160	BiOF	3.3538	0.00000025
mp-570443	Tl2CN2	1.892	2.33333E-07
mp-11508	MoP4	0	0.0000002

Continued on next page

Table 5.3 – continued from previous page

MPID	Material Formula	Band Gap(eV)	Total Magnetization (A/m)
mp-555760	S	2.2718	1.88889E-07
mp-568388	BiI	0.8279	0.000000175
mp-8187	K2ZnO2	1.9785	0.00000015
mp-769016	Pb(BrO3)2	3.2535	0.00000015
mp-27480	Sn2OF2	2.6708	0.00000015
mp-616327	In3Te3I	1.1004	0.00000005
mp-5770	AgNO2	1.7726	0
mp-942	AuF3	1.4723	0
mp-30097	Bi2Te7Cl8	0.7625	0
mp-23324	BiSBr	2.0287	0
mp-23318	BiSCl	1.9601	0
mp-569707	BiSeBr	1.6912	0
mp-23020	BiSeI	1.5745	0
mp-23514	BiSI	1.8669	0
mp-27724	BPS4	2.2625	0
mp-3199	CuSe2O5	0.0055	0
mp-27218	Ge(BrF5)2	2.9044	0

Continued on next page

Table 5.3 – continued from previous page

MPID	Material Formula	Band Gap(eV)	Total Magnetization (A/m)
mp-568616	Nb2Br5	0.709	0
mp-541817	NbSeI3	0.6281	0
mp-559792	Nd2As6Xe5F46	2.6927	0
mp-19727	PbCN2	1.7031	0
mp-560008	PNF2	5.6175	0
mp-558576	ReSb(OF4)2	3.7699	0
mp-22996	SbSeI	1.3776	0
mp-14	Se	0.9988	0
mp-29174	SiCl2	2.0151	0
mp-1602	SiS2	3.0676	0
mp-568264	SiSe2	2.1493	0
mp-17835	Sn2Sb2S5	1.045	0
mp-19	Te	0.1856	0
mp-582657	Ti4Te9I4O	0.3978	0
mp-574169	TiGeTe6	0.4183	0
mp-720	TlF	3.2045	0

5.2 Band gap prediction and magnetic material classification

The starting point of machine learning is choosing a proper model. Optimized distributed gradient boosting (XGBoost) is the leading model for working with standard tabular data, such as dataframe, json, csv and excel. This model dominates many Kaggle competitions. It is an implementation of the Gradient Boosted Decision Trees algorithm. Comparing with other machine learning algorithms, it has better accuracy. Comparing with deep learning it allows much better interpretation.

Feature engineering is the process of using domain knowledge of the data to create features that make machine learning algorithms work. It is fundamental to the application of machine learning, and is both difficult and expensive. The purpose is to find out those features that can help when solving the problem, and encode them into the format that the model can read. In this study, two kinds of features have been selected: structural features and elemental features. The structural features are originate from the information of the unit cell such as the unit cell volume and the number of the atoms. While the elemental features originate from the information of periodic table such as atomic weight, atomic radius, and number of valence electrons. For the best performance, the average, min/max values and differences of each elemental feature have been calculated. For non-numerical features, such as space group, we did one-hot-encoding (OHT) since it is necessary for XGBoost. In total, 20,000 kinds of different materials have been included in the machine learning. The 20,000 materials have been divided into two subsets: 75 % training samples (15,000) and 25 % testing samples (5,000). For each material there are 95 features included. they will be used to predict band gap and to do magnetic material classification.

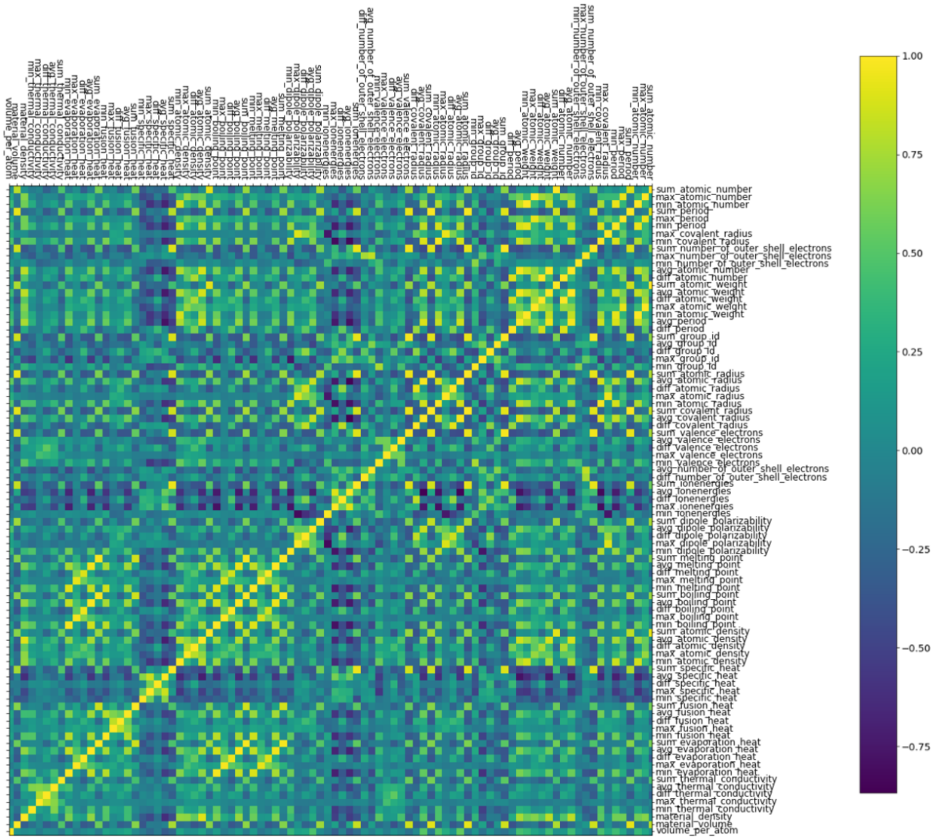

Figure 5.2: The correlation heat map of all the features considered in the XGBoost, yellow indicates that two features are positively linear correlated, while dark green indicates that two feature are negatively linear correlated.

Fig. 5.2 shows the feature correlation heat map. The yellow square indicates that the corresponding two features are positively correlated. While the dark green indicates that the corresponding two features are negatively correlated. Those features with 0 correlation mean that they are not correlated. Those highly correlated features are used to fill in the missing values in elemental features.

Table 5.4: The predicted band gap vs band gap from MPDB.

Material Formula	**Predicted Band Gap (eV)**	**Band Gap from MPDB (eV)**
Ce3(AgGe)4	0.002	0
SrCaMg30O32	4.239	4.431
Li3V(H4O3)4	3.994	4.026
ZnPb2F6	4.004	3.923
Cr3N4	0	0
CsLi2F3	6.78	7.04
Ni3Sn2	0.004	0
V2Cu2O7	0.016	0
Li2Mn3TeO8	0.226	0
MgH10CO8	4.818	4.795
ReH4NO4	3.926	4.086
BaTi8O16	0	0
LiB(SO4)2	6.145	6.387
KGaH4	4.951	4.936
ThMn4(CuO4)3	0	0
CaSbPt	0	0
Sc2IrPd	0.223	0

Continued on next page

Table 5.4 – continued from previous page

Material Formula	**Predicted Band Gap(eV)**	**Band Gap from MPDB (eV)**
Cu	0.024	0
Rb2Be3Zn2F12	5.895	5.858
KSm(PO3)4	5.402	5.297
Mn3W3C	0.009	0
K2LiDyCl6	4.95	5.02
Na3YC2(O3F)2	5.014	4.884
Li5GaO4	3.08	3.763
CsNaB10(H2O9)2	5.421	5.762
Gd6Ta4Al43	0.052	0

Before running XGBoost, the last step we need to do is a parameter grid search. For more details, please refer to Sec. A.2 of the Appendix. Table 5.4 shows a subset of the central results of band gap prediction, the comparison between the predicted band gap and band gap obtained from MPDB. The calculated mean absolute error of the training samples is 0.148 eV, which prove that our prediction is in good agreement with the results on MPDB. For the magnetic material classification, the results accuracy can be evaluated by the confusion matrix as shown in Fig. 5.3. Among 5000 kinds of materials, our model found 1315 magnetic materials and 3685 non-magnetic materials, in reality, there are 1155 magnetic materials and 3845 non-magnetic materials. The accuracy can be calculated by:

$$accuracy = \frac{TP + TN}{TP + TN + FP + FN} \tag{5.1}$$

where TP refers to true positive which means the number of the materials are actual magnetic material has also been predicted as magnetic material. While FN refers to false negative which means the number of the materials are actual magnetic material but has been predicted as non-magnetic material. The smaller the values of FP and FN, the better the accuracy is. When the values of FP and FN both equal to 0, the accuracy is 1. In this study, the accuracy is 0.916.

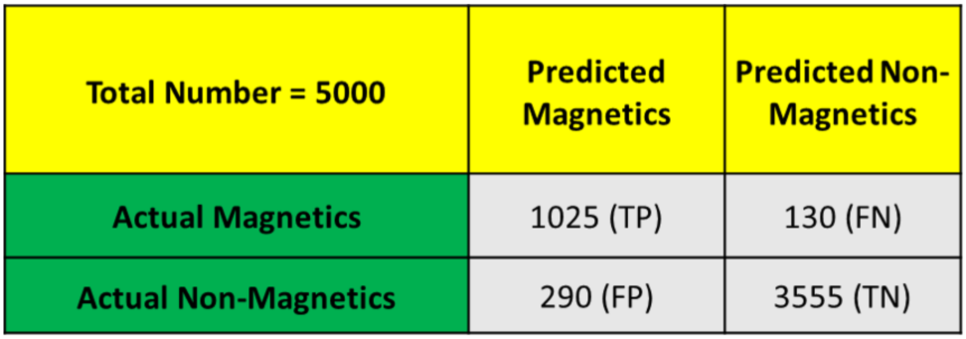

Total Number = 5000	**Predicted Magnetics**	**Predicted Non-Magnetics**
Actual Magnetics	1025 (TP)	130 (FN)
Actual Non-Magnetics	290 (FP)	3555 (TN)

Figure 5.3: Confusion matrix of magnetic material classification, used to judge the accuracy of the classification.

To evaluate which feature dominates the prediction and classification, the most important 10 features are shown in Fig. 5.4. The feature importance criteria we used is "gain". "Gain" indicates the improvement in accuracy brought by a feature to the branches it is on. It is the most widely used criteria to evaluate the feature importance. For band gap prediction, the maximum value of the elemental valence electrons is the most important feature. For magnetic material classification, the maximum value of the elemental period is the most important feature.

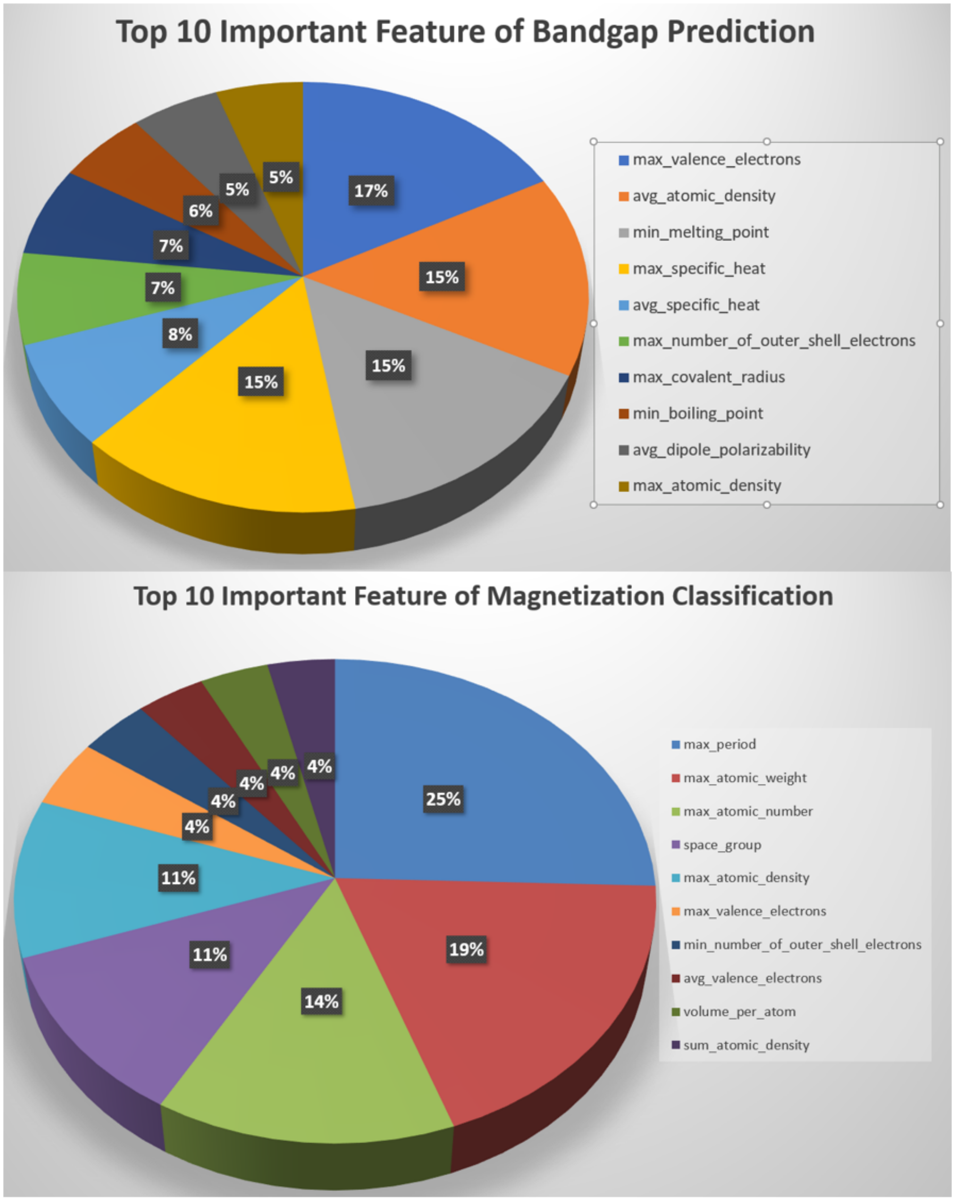

Figure 5.4: The most important 10 features for predicting band gap and for magnetic material classification.

Chapter 6

Summary and Outlook

In conclusion, the dependence of the in-plane thermal conductivity of TBG is theoretically investigated. For large commensurate rotation angles ($< 13.2^\circ$), the thermal conductivities decrease approximately linearly with the increasing lattice. At a commensurate lattice constant of 1.1 nm corresponding to an angle of 13.2°, the thermal conductivity falls to 50% of the value of the aligned AB structure at room temperature. For all 13 commensurate rotation angles we considered, rotation does not affect the phonon velocities or frequencies, but it does reduce the Brillouin zone size to the extent that the zone edge acoustic phonon energies are thermally populated. This allows Umklapp scattering to reduce the lifetimes of the phonons contributing to the thermal transport and, consequently, to reduce the thermal conductivity. The DFT calculations give solid proof for this explanation by observing a reduction of the phonon lifetimes in TBG compared to AB-BLG.

For small commensurate rotation angles ($> 13.2^\circ$), a non-monotonic dependence of the thermal conductivity on the commensurate lattice constant has been discovered. As the commensurate lattice constant increases, the in-plane thermal conductivity increases and reaches 91% of the AB value at a commensurate lattice constant of 7.5 nm corresponding to an angle of 1.89°. The commensurate-lattice-constant-dependent trends in the thermal conductivity are also followed by the trends in the shear elastic constant C_{44}, the wrinkling intensity, and the frequency of the out-of-plane ZA_2 mode. The picture that emerges from these results is that the interlayer misorientation reduces the shear elastic constant C_{44}, the reduced shear elastic constant allows increased wrinkling of the TBG, and the increased wrinkling reduces the thermal conductivity.

The small-angle approach of the thermal conductivity towards its value in the aligned structure raises the question of how response functions approach their aligned values as the twist angle approaches 0°. Is the approach gradual, discontinuous, or a combination of the two?

To identify quasi-1D material from 2D material, an improved dimension classifier model has been created. The algorithm of this model is based on the fact that quasi-1D material contains different bond lengths in the unit cell. The accuracy of this model is validated by successfully identifying known quasi-1D material based on the structural data from MPDB. Using structural data and elemental properties from MPDB, we perform a band gap prediction and magnetic material classification by applying XGBoost model. By fitting the XGBoost model with 15,000 kinds of materials, the accuracy of the predictions on the 5000 testing samples is greater than 91%. The MAE of the band gap prediction is 0.148 eV. For the magnetic material classification, 1,025 kinds of magnetic materials and 3,555 kinds non-magnetic materials have been identified. Using gain as the criteria, the most correlated feature for band gap prediction is the number of the valence electrons. While, for the magnetic material classification, it is the elemental period.

Chapter 7

Appendix

A.1 Band Gap Prediction using Machine Learning (Python3)

The first step of machine learning is downloading data from material project databases and format them. To do this you can use the following code, some packages might need to install before running, such as pymatgen, mendeleev, numpy and pandas.

```
from pymatgen import MPRester, Composition
from pymatgen.electronic_structure.plotter import BSPlotter
import pymatgen.analysis.find_dimension
import pymatgen.io.cif as pcif
import pandas as pd
from tqdm import tqdm
#import periodictable as pt
from mendeleev import element
import re
```

```
import numpy as np
from collections import OrderedDict
from IPython.display import clear_output
import time

def get_valence(group_id):
    if group_id == None:
        return(None)
    elif group_id >= 1 and group_id <= 12:
        return(group_id)
    elif group_id >= 13 and group_id <= 18:
        return(group_id-10)
    elif group_id ==0:
        return(8)
    else:
        raise ValueError('The␣group␣ID␣is␣out␣of␣range')

def NumberOfElement(unit_cell_formula,element):
    if element not in unit_cell_formula:
        raise ValueError('Element␣can␣not␣be␣found␣in␣pretty_formula')
    else:
        return(unit_cell_formula[element])

NumberOfElement({'C': 2.0, 'P': 2.0, 'V': 4.0},'C')+1

def getOneElementFeature(feature, Element):
    currentElem = element(Element)
```

```
if feature == "atomic_number":

    return(currentElem.atomic_number)


elif feature == "atomic_weight":

    return(currentElem.atomic_weight)


elif feature == "period":

    return(currentElem.period)


elif feature == "group_id":

    return(currentElem.group_id)


elif feature == "atomic_radius":

    return(currentElem.atomic_radius)


elif feature == "covalent_radius":

    return(currentElem.covalent_radius)


elif feature == "valence_electrons":

    return(get_valence(currentElem.group_id))


elif feature == "number_of_outer_shell_electrons":

    d = OrderedDict(currentElem.ec.electrons_per_shell())

    els = list(d.items())

    return(list(d.items())[-1][1])
```

```
elif feature == "ionenergies":
    return(currentElem.ionenergies[1])

elif feature == "dipole_polarizability":
    return(currentElem.dipole_polarizability)

elif feature == "melting_point":
    return(currentElem.melting_point)

elif feature == "boiling_point":
    return(currentElem.boiling_point)

elif feature == "atomic_density":
    return(currentElem.density)

elif feature == "specific_heat":
    return(currentElem.specific_heat)

elif feature == "fusion_heat":
    return(currentElem.fusion_heat)

elif feature == "evaporation_heat":
    return(currentElem.evaporation_heat)

elif feature == "thermal_conductivity":
    return(currentElem.thermal_conductivity)
```

```
    else:
        raise ValueError('This␣feature␣dose␣not␣exsits')



def createElementsDict(unit_cell_formula):
    return(unit_cell_formula)



def natoms(unit_cell_formula,elements):
    n = 0
    for element in elements:
        n += NumberOfElement(unit_cell_formula, element)
    return(n)

def featureSum(feature, unit_cell_formula, elements):
    fsum = 0
    elements_dict = createElementsDict(unit_cell_formula)
    for Element in elements:
        fsum += getOneElementFeature(feature,Element)*elements_dict[Element]
    return(fsum)

def featureAvg(feature, unit_cell_formula, elements):
    return(featureSum(feature, unit_cell_formula, elements)/natoms(
       unit_cell_formula,elements))

def featureDifference(feature, unit_cell_formula, elements):
    favg = featureAvg(feature, unit_cell_formula, elements)
```

```
    fdiff = 0
    for Element in elements:
        fdiff +=  (getOneElementFeature(feature,Element) - favg)**2
    return(np.sqrt(fdiff/natoms(unit_cell_formula,elements)))

def featureLargest(feature, unit_cell_formula, elements):
    feature_values = []
    for Element in elements:
        feature_values.append(getOneElementFeature(feature,Element))
    return(max(feature_values))

def featureSmallest(feature, unit_cell_formula, elements):
    feature_values = []
    for Element in elements:
        feature_values.append(getOneElementFeature(feature,Element))
    return(min(feature_values))

featureSum("atomic_weight",{'Rb': 2.0, 'Te': 2.0, 'Au': 2.0}
,['Rb','Te','Au'])

atomicFeatures = ["atomic_number","atomic_weight","period","group_id","
    atomic_radius","covalent_radius","valence_electrons",                  "
    number_of_outer_shell_electrons","ionenergies","dipole_polarizability","
    melting_point","boiling_point",                     "atomic_density","
    specific_heat","fusion_heat","evaporation_heat","thermal_conductivity"]
```

```
len(atomicFeatures)

mpr = MPRester("Frv0akZ1InOToUmL")##API key should be inside the "", URL for
    API key: https://materialsproject.org/dashboard
data = mpr.query(criteria={"band_gap": {"$gt": -0.1}},properties=(["cif","
    pretty_formula","unit_cell_formula","band_gap","volume","spacegroup","
    density","elements","nelements"]))

pd_all = pd.DataFrame(data)

pd_all.head(20)

pd_all['spacegroup'][4]['crystal_system']

pd_all.query('band_gap␣==␣0').shape

pd_subset = pd.concat([pd_all.query('band_gap␣==␣0')[0:10],pd_all.query('
    band_gap␣!=␣0')[-10::]])

pd_subset.shape

pd_subset.head()

pd_subset.isnull().sum()

pd_subset.reset_index(inplace=True)
```

```
dict_all = {}
for i in range(len(atomicFeatures)):
    dict_all["sum_"+atomicFeatures[i]] = []
    dict_all["avg_"+atomicFeatures[i]] = []
    dict_all["diff_"+atomicFeatures[i]] = []
    dict_all["max_"+atomicFeatures[i]] = []
    dict_all["min_"+atomicFeatures[i]] = []
    for j in range(pd_subset.shape[0]):
        feature_tester = []          #test whether there is None feature value
        for Element in pd_subset['elements'][j]:
            feature_tester.append(getOneElementFeature(atomicFeatures[i],
                Element))
        if None not in feature_tester:
            clear_output()
            print("row␣"+ str(j) + "␣and␣feature␣" + str(i))
            dict_all["sum_"+atomicFeatures[i]].append(featureSum(
                atomicFeatures[i],pd_subset['unit_cell_formula'][j],pd_subset[
                'elements'][j]))
            dict_all["avg_"+atomicFeatures[i]].append(featureAvg(
                atomicFeatures[i],pd_subset['unit_cell_formula'][j],pd_subset[
                'elements'][j]))
            dict_all["diff_"+atomicFeatures[i]].append(featureDifference(
                atomicFeatures[i],pd_subset['unit_cell_formula'][j],pd_subset[
                'elements'][j]))
            dict_all["max_"+atomicFeatures[i]].append(featureLargest(
                atomicFeatures[i],pd_subset['unit_cell_formula'][j],pd_subset[
                'elements'][j]))
```

```
            dict_all["min_"+atomicFeatures[i]].append(featureSmallest(atomicFeatures[i],pd_subset['unit_cell_formula'][j],pd_subset['elements'][j]))
        else:
            dict_all["sum_"+atomicFeatures[i]].append('None')
            dict_all["avg_"+atomicFeatures[i]].append('None')
            dict_all["diff_"+atomicFeatures[i]].append('None')
            dict_all["max_"+atomicFeatures[i]].append('None')
            dict_all["min_"+atomicFeatures[i]].append('None')

pd.DataFrame(pd.DataFrame(dict_all)=='None').sum()


dict_all["band_gap"] = []
dict_all["material_density"] = []
dict_all["material_volume"] = []
dict_all["space_group"] = []
dict_all["volume_per_atom"] = []
dict_all["pretty_formula"] = []
dict_all['unit_cell_formula'] = []
dict_all["cif"] = []
for i in range(pd_subset.shape[0]):
    clear_output()
    natom = 0
    for Element in pd_subset['elements'][i]:
        natom += NumberOfElement(pd_subset['unit_cell_formula'][i],Element)
    dict_all["band_gap"].append(pd_subset['band_gap'][i])
    dict_all["material_density"].append(pd_subset['density'][i])
```

```
    dict_all["material_volume"].append(pd_subset['volume'][i])
    dict_all["space_group"].append(pd_subset["spacegroup"][i]['crystal_system'
        ])
    dict_all["volume_per_atom"].append(pd_subset["volume"][i]/natom)
    dict_all["pretty_formula"].append(pd_subset["pretty_formula"][i])
    dict_all['unit_cell_formula'].append(pd_subset['unit_cell_formula'][i])
    dict_all["cif"].append(pd_subset["cif"][i])
    print("row␣"+ str(i))

ML_data = pd.DataFrame(dict_all)
ML_data.to_excel("ML_data_20.xlsx")
```

After this step we need to clean the data, in this project, what we did is imputing the missing data according to the known part of the data. You can run the following code in the same directory, changing the ".xlsx" file name accordingly. Although we did not plot the distribution of each feature in this step, it is still recommended to do it. Because most of machine learning algorithms are based on the assumption that the feature values are normally distributed. If not, a feature engineering need to be done before applying machine learning.

```
import pandas as pd
import numpy as np
from sklearn.impute import SimpleImputer
from sklearn.experimental import enable_iterative_imputer
from sklearn.impute import IterativeImputer
pd_all = pd.read_excel('ML_data_10000.xlsx')
```

```
pd_all.replace('None',-999,inplace=True)
numerics = ['int16', 'int32', 'int64', 'float16', 'float32', 'float64']
numeric_columns = pd_all.select_dtypes(include=numerics).columns
non_numeric_columns = pd_all.select_dtypes(exclude=numerics).columns
# fitting the missing data using mean value algorithm
imp = SimpleImputer(missing_values=-999, strategy='mean')
imp.fit(pd_all.select_dtypes(include=numerics))
df_numeric = pd.DataFrame(imp.transform(pd_all.select_dtypes(include=numerics)
    ),columns=numeric_columns)
df_nonnumeric = pd_all.select_dtypes(exclude=numerics)
pd.merge(df_numeric, df_nonnumeric, left_index=True, right_index=True).
    to_excel('ML_data_impute_10000.xlsx')
# fitting the missing data using predictions
imp_feature = IterativeImputer(max_iter=100, random_state=0,missing_values
    =-999,initial_strategy='most_frequent')
imp_feature.fit(pd_all.select_dtypes(include=numerics))
df_numeric_2 = pd.DataFrame(imp_feature.transform(pd_all.select_dtypes(include
    =numerics)),columns=numeric_columns)
pd.merge(df_numeric_2, df_nonnumeric, left_index=True, right_index=True).
    to_excel('ML_data_impute_5_10000.xlsx')
```

The last step is fitting the data into the selected machine learning model and using them to do the prediction. The optimized distributed gradient boosting (XGB) is applied in this code. As the regularized version of gradient boosting method, XGB is an efficient and easy to use algorithm. It delivers high performance and accuracy as compared to other algorithms.

To measure the accuracy of the prediction, we could split the data (have both features and targets) into two samples: training and testing. Only training samples will be fitted, and testing samples are only used to judge the accuracy. Run the following code will automatically generate a ".xlsx" file with predicted bandgap of 5000 materials. The mean absolute error of the prediction is only 0.148 eV.

```
import pandas as pd
import numpy as np
import xgboost as xgb
import seaborn as sns
from sklearn.model_selection import KFold,GridSearchCV
from sklearn.ensemble import ExtraTreesRegressor
from sklearn.ensemble import RandomForestRegressor
from sklearn import metrics, preprocessing
from sklearn.model_selection import cross_validate
from sklearn.model_selection import train_test_split
import time
import matplotlib.pyplot as plt
from scipy import sparse
from sklearn.metrics import mean_absolute_error
get_ipython().run_line_magic('matplotlib', 'inline')


## Load Data
df_all = pd.read_excel('ML_data_FeatureImpute_0to10000.xlsx')
df_all.head()
ml_all = df_all.drop(columns=['Unnamed:␣0','Unnamed:␣0.1','pretty_formula','
    unit_cell_formula','cif'])
```

```
data_types = ml_all.dtypes
cat_cols = list(data_types[data_types=='object'].index)
con_cols = list(data_types[data_types=='int64'].index) + list(data_types[
    data_types=='float64'].index)
con_cols.remove('band_gap')
print ("Categorical␣features:", cat_cols)
print ( "Numerica␣features:", con_cols)

## Encode cat features, must do before using XGB
OHE = preprocessing.OneHotEncoder(sparse=True)
start=time.time()
full_data_sparse=OHE.fit_transform(ml_all[cat_cols])
print ('One-hot-encoding␣finished␣in␣%f␣seconds' % (time.time()-start))
full_data_sparse = sparse.hstack((full_data_sparse,ml_all[con_cols]), format='
    csr')

## Train test split
train_x,test_x,train_y,test_y = train_test_split(full_data_sparse, ml_all['
    band_gap'], test_size=0.25, random_state=42)

## Metod for evaluation
def logregobj(labels, preds):
    con = 2
    x =preds-labels
    grad =con*x / (np.abs(x)+con)
    hess =con**2 / (np.abs(x)+con)**2
    return grad, hess
```

```
def log_mae(y,yhat):
    return mean_absolute_error(np.exp(y), np.exp(yhat))

log_mae_scorer = metrics.make_scorer(log_mae, greater_is_better = False)

## Grid Search for the best model
def search_model(train_x, train_y, est, param_grid, n_jobs, cv, refit=False):
    model = GridSearchCV(estimator  = est,
                                     param_grid = param_grid,
                                     scoring    = log_mae_scorer,
                                     verbose    = 10,
                                     n_jobs   = n_jobs,
                                     iid        = True,
                                     refit     = refit ,
                                     cv       = cv)
    # Fit Grid Search Model
    model.fit(train_x, train_y)
    print("Best score: %0.3f" % model.best_score_)
    print("Best parameters set:", model.best_params_)
    print("Scores:", model.cv_results_)
    return model


param_grid = {'objective':[logregobj],
              'learning_rate':[0.03,0.1,0.2],
              'n_estimators':[2000,4000,8000],
```

```
              'max_depth': [6,8,10],
              'min_child_weight':[10,8,6,4,2,1],
              'subsample': [0.78,0.5],
              'colsample_bytree':[0.67],
              'gamma':[0,0.9,10],
              'nthread': [-1],
              'seed' : [1234]}

model = search_model(train_x,
                     train_y,
                     xgb.XGBRegressor(),
                     param_grid,
                     n_jobs = 1,
                     cv = 4,
                     refit = True)

## Setting up the paramters of XGB and fitting the model
rgr = xgb.XGBRegressor(seed = 1234,
                       learning_rate = 0.03, # smaller, better results, more
                           time
                       n_estimators = 2000, # Number of boosted trees to fit.
                       max_depth=10, # the maximum depth of a tree
                       min_child_weight=10,
                       colsample_bytree=0.67, # the fraction of columns to be
                           randomly samples for each tree
                       subsample=0.78, # the fraction of observations to be
                           randomly samples for each tree
```

```
                       gamma=0.9, # Minimum loss reduction required to make a
                           further partition on a leaf node of the tree,
                       # the larger, the more conservative
                       nthread = -1, # Number of parallel threads used to run
                           xgboost.
                       silent = False # Whether to print messages while
                           running boosting.
                      )
rgr.fit(train_x, train_y)

## Predict the bandgap using the fitted model
pred_y = rgr.predict(test_x)

## Save prediction results of test samples
results = pd.DataFrame()
results['pretty_formula'] = df_all.iloc[test_y.index]['pretty_formula']
results['band_gap'] = pred_y
results['real_band_gap'] = test_y.values
results.to_excel("pred_20191118.xlsx", index=False)

## Print MAE of test sample prediction unit eV
print(mean_absolute_error(pred_y, test_y.values))



## Save prediction results for train samples, used to check overfitting
pred_train_y = rgr.predict(train_x)
results = pd.DataFrame()
```

```
results['pretty_formula'] = df_all.iloc[train_y.index]['pretty_formula']
results['band_gap'] = pred_train_y
results['real_band_gap'] = train_y.values
results.to_excel("pred_20191118_train.xlsx", index=False)
mean_absolute_error(pred_train_y, train_y.values)

## plot the feature importance
xgb.plot_importance(rgr,max_num_features=10,importance_type='gain')
```

If you want to try predicting the total magnetization, you need to include "total_magnetization" into your mpr query. Also you need to drop the "total_magnetization" from the continues features. The two lines you need to revise in the code are as below:

```
...
data = mpr.query(criteria={"band_gap": {"$gt": -0.1}},properties=(["cif","
    pretty_formula","unit_cell_formula","band_gap","volume","spacegroup","
    density","elements","nelements","total_magnetization"]))
...
...
...
con_cols.remove('total_magnetization')
...
```

A.2 Dimension Classifier (Python3)

This code is used to classify the dimension of a given material into the one of the following types: 0D, 1D, quasi-1D, 2D, 3D, intercalated ion and intercalated molecule. The code used the find_dimension package implemented in pymatgen. It needs the structure files with ".cif" format as input, and output a spreadsheet with three columns: formula of the material, dimension of the material and band gap. The band gap information is directly downloaded from material project.

To use this code, you need to adjust the tolerance before running it. If the tolerance is too big, some "quasi-1D" materials will be identified as 2D material, while if it is too small, some of them will be identified as 0D material or intercalated ion.

```
from pymatgen import MPRester, Composition
from pymatgen.electronic_structure.plotter import BSPlotter
import pymatgen.analysis.find_dimension
import pymatgen.io.cif as pcif
import pandas as pd
import pymatgen.analysis.find_dimension as pfd
from tqdm import tqdm

######Loading data from material projects
mpr = MPRester("Frv0akZ1InOToUmL")##API key should be inside the "", URL for API key: https://materialsproject.org/dashboard
data = mpr.query(criteria={"band_gap": {"$gt": -0.1}},properties=(["cif","pretty_formula","unit_cell_formula","band_gap","volume","spacegroup","density","elements","nelements"]))
df_all = pd.DataFrame(data)
df_all.to_excel('Material_Project_dataForDimensionClassify.xlsx')

######Prepare Input Files
```

```
subsample = 100
for i in range(len(data[:subsample])):
    with open(str(i) + '_dimension.cif', 'w') as the_file:
        the_file.write(data[i]['cif'])

#####Dimension Classification
dimensions = []
for i in tqdm(range(len(data[:subsample]))):
    dim = pfd.find_dimension(pcif.Structure.from_file(str(i)+"_dimension.cif")
        )
    if dim == '2D' and  pfd.find_dimension(pcif.Structure.from_file(str(i)+"
        _dimension.cif"),tolerance=0.1) == "1D":
        dimensions.append('quasi-1D')
    else:
        dimensions.append(dim)
#####Generate Outputs
pretty_formula = []
band_gap = []
for i in range(len(data[:subsample])):
    pretty_formula.append(data[i]['pretty_formula'])
    band_gap.append(data[i]['band_gap'])
df_dimensions = pd.DataFrame({'pretty_formula':pretty_formula,'band_gap':
    band_gap,'dimensions':dimensions})
df_dimensions.to_excel('df_dimensions.xlsx')
```

Bibliography

[1] Chenyang Li, Bishwajit Debnath, Xiaojian Tan, Shanshan Su, Kui Xu, Supeng Ge, Mahesh R Neupane, and Roger K Lake. Commensurate lattice constant dependent thermal conductivity of misoriented bilayer graphene. *Carbon*, 138:451–457, 2018.

[2] Chenyang Li and Roger K Lake. Small angle and non-monotonic behavior of the thermal conductivity in twisted bilayer graphene. *Carbon*, under review, 2019.

[3] John Towns, Timothy Cockerill, Maytal Dahan, Ian Foster, Kelly Gaither, Andrew Grimshaw, Victor Hazlewood, Scott Lathrop, Dave Lifka, Gregory D Peterson, et al. Xsede: accelerating scientific discovery. *Computing in Science & Engineering*, 16(5):62–74, 2014.

[4] Byoung Don Kong, S Paul, M Buongiorno Nardelli, and Ki Wook Kim. First-principles analysis of lattice thermal conductivity in monolayer and bilayer graphene. *Physical Review B*, 80(3):033406, 2009.

[5] C Oshima, T Aizawa, R Souda, Y Ishizawa, and Y Sumiyoshi. Surface phonon dispersion curves of graphite (0001) over the entire energy region. *Solid State Communications*, 65(12):1601–1604, 1988.

[6] H Yanagisawa, T Tanaka, Y Ishida, M Matsue, E Rokuta, S Otani, and C Oshima. Analysis of phonons in graphene sheets by means of hreels measurement and ab initio calculation. *Surface and interface analysis*, 37(2):133–136, 2005.

[7] J Maultzsch, S Reich, C Thomsen, H Requardt, and P Ordejón. Phonon dispersion in graphite. *Physical review letters*, 92(7):075501, 2004.

[8] AH Castro Neto, Francisco Guinea, Nuno MR Peres, Kostya S Novoselov, and Andre K Geim. The electronic properties of graphene. *Reviews of modern physics*, 81(1):109, 2009.

[9] IW Frank, David M Tanenbaum, Arend M van der Zande, and Paul L McEuen. Mechanical properties of suspended graphene sheets. *Journal of Vacuum Science & Technology B: Microelectronics and Nanometer Structures Processing, Measurement, and Phenomena*, 25(6):2558–2561, 2007.

[10] LA Falkovsky. Optical properties of graphene. In *Journal of Physics: Conference Series*, volume 129, page 012004. IOP Publishing, 2008.

[11] Andre K Geim and Konstantin S Novoselov. The rise of graphene. In *Nanoscience and Technology: A Collection of Reviews from Nature Journals*, pages 11–19. World Scientific, 2010.

[12] Alexander A Balandin. Thermal properties of graphene and nanostructured carbon materials. *Nature materials*, 10(8):569, 2011.

[13] Khan MF Shahil and Alexander A Balandin. Graphene–multilayer graphene nanocomposites as highly efficient thermal interface materials. *Nano letters*, 12(2):861–867, 2012.

[14] Chih-Jen Shih, Aravind Vijayaraghavan, Rajasekar Krishnan, Richa Sharma, Jae-Hee Han, Moon-Ho Ham, Zhong Jin, Shangchao Lin, Geraldine LC Paulus, Nigel Forest Reuel, et al. Bi-and trilayer graphene solutions. *Nature Nanotechnology*, 6(7):439, 2011.

[15] Hongyang Li, Hao Ying, Xiangping Chen, Denis L Nika, Alexandr I Cocemasov, Weiwei Cai, Alexander A Balandin, and Shanshan Chen. Thermal conductivity of twisted bilayer graphene. *Nanoscale*, 6(22):13402–13408, 2014.

[16] Zhiyong Wei, Zhonghua Ni, Kedong Bi, Minhua Chen, and Yunfei Chen. In-plane lattice thermal conductivities of multilayer graphene films. *Carbon*, 49(8):2653–2658, 2011.

[17] Alexandr I Cocemasov, Denis L Nika, and Alexander A Balandin. Phonons in twisted bilayer graphene. *Physical Review B*, 88(3):035428, 2013.

[18] Jessica Campos-Delgado, Luiz G Cançado, Carlos A Achete, Ado Jorio, and Jean-Pierre Raskin. Raman scattering study of the phonon dispersion in twisted bilayer graphene. *Nano Research*, 6(4):269–274, 2013.

[19] Alexander A Balandin, Suchismita Ghosh, Wenzhong Bao, Irene Calizo, Desalegne Teweldebrhan, Feng Miao, and Chun Ning Lau. Superior thermal conductivity of single-layer graphene. *Nano letters*, 8(3):902–907, 2008.

[20] Jackie D Renteria, Denis L Nika, and Alexander A Balandin. Graphene thermal properties: applications in thermal management and energy storage. *Applied Sciences*, 4(4):525–547, 2014.

[21] Xiaojian Tan, Hezhu Shao, Tianqi Hu, Guoqiang Liu, Jun Jiang, and Haochuan Jiang. High thermoelectric performance in two-dimensional graphyne sheets predicted by first-principles calculations. *Physical Chemistry Chemical Physics*, 17(35):22872–22881, 2015.

[22] Suchismita Ghosh, Wenzhong Bao, Denis L Nika, Samia Subrina, Evghenii P Pokatilov, Chun Ning Lau, and Alexander A Balandin. Dimensional crossover of thermal transport in few-layer graphene. *Nature materials*, 9(7):555, 2010.

[23] L Lindsay, DA Broido, and Natalio Mingo. Diameter dependence of carbon nanotube thermal conductivity and extension to the graphene limit. *Physical Review B*, 82(16):161402, 2010.

[24] Bo Qiu and Xiulin Ruan. Mechanism of thermal conductivity reduction from suspended to supported graphene: a quantitative spectral analysis of phonon scattering. In *ASME 2011 International Mechanical Engineering Congress and Exposition*, pages 303–313. American Society of Mechanical Engineers, 2011.

[25] Hengji Zhang, Geunsik Lee, and Kyeongjae Cho. Thermal transport in graphene and effects of vacancy defects. *Physical Review B*, 84(11):115460, 2011.

[26] Chenyang Li, Ling Miao, Xiaojian Tan, Mengdi Han, and Jianjun Jiang. Thermal conductivity of graphene nanoribbons with regular isotopic modification. *Journal of Computational and Theoretical Nanoscience*, 11(2):348–352, 2014.

[27] dS Ghosh, I Calizo, D Teweldebrhan, Evghenii P Pokatilov, Denis L Nika, Alexander A Balandin, Wenzhong Bao, Feng Miao, and C Ning Lau. Extremely high thermal conductivity of graphene: Prospects for thermal management applications in nanoelectronic circuits. *Applied Physics Letters*, 92(15):151911, 2008.

[28] Victor Carozo, Clara M Almeida, Erlon HM Ferreira, Luiz Gustavo Cancado, Carlos Alberto Achete, and Ado Jorio. Raman signature of graphene superlattices. *Nano letters*, 11(11):4527–4534, 2011.

[29] Robin W Havener, Houlong Zhuang, Lola Brown, Richard G Hennig, and Jiwoong Park. Angle-resolved raman imaging of interlayer rotations and interactions in twisted bilayer graphene. *Nano letters*, 12(6):3162–3167, 2012.

[30] Kwanpyo Kim, Sinisa Coh, Liang Z Tan, William Regan, Jong Min Yuk, Eric Chatterjee, MF Crommie, Marvin L Cohen, Steven G Louie, and A Zettl. Raman spectroscopy study of rotated double-layer graphene: misorientation-angle dependence of electronic structure. *Physical review letters*, 108(24):246103, 2012.

[31] Rui He, Ting-Fung Chung, Conor Delaney, Courtney Keiser, Luis A Jauregui, Paul M Shand, CC Chancey, Yanan Wang, Jiming Bao, and Yong P Chen. Observation of low energy raman modes in twisted bilayer graphene. *Nano letters*, 13(8):3594–3601, 2013.

[32] Chun Hung Lui, Leandro M Malard, SukHyun Kim, Gabriel Lantz, François E Laverge, Riichiro Saito, and Tony F Heinz. Observation of layer-breathing mode vibrations in few-layer graphene through combination raman scattering. *Nano letters*, 12(11):5539–5544, 2012.

[33] Sinisa Coh, Liang Z Tan, Steven G Louie, and Marvin L Cohen. Theory of the raman spectrum of rotated double-layer graphene. *Physical Review B*, 88(16):165431, 2013.

[34] A Righi, P Venezuela, H Chacham, SD Costa, C Fantini, RS Ruoff, L Colombo, WS Bacsa, and MA Pimenta. Resonance raman spectroscopy in twisted bilayer graphene. *Solid State Communications*, 175:13–17, 2013.

[35] Pankaj Ramnani, Mahesh R Neupane, Supeng Ge, Alexander A Balandin, Roger K Lake, and Ashok Mulchandani. Raman spectra of twisted cvd bilayer graphene. *Carbon*, 123:302–306, 2017.

[36] V Perebeinos, J Tersoff, and Ph Avouris. Phonon-mediated interlayer conductance in twisted graphene bilayers. *Physical review letters*, 109(23):236604, 2012.

[37] GSN Eliel, MVO Moutinho, AC Gadelha, A Righi, LC Campos, HB Ribeiro, Po-Wen Chiu, K Watanabe, T Taniguchi, P Puech, et al. Intralayer and interlayer electron–phonon interactions in twisted graphene heterostructures. *Nature communications*, 9(1):1221, 2018.

[38] Wang Min-Hua, Xie Yue-E, and Chen Yuan-Ping. Thermal transport in twisted few-layer graphene. *Chinese Physics B*, 26(11):116503, 2017.

[39] Alexandr I Cocemasov, Denis L Nika, and Alexander A Balandin. Engineering of the thermodynamic properties of bilayer graphene by atomic plane rotations: the role of the out-of-plane phonons. *Nanoscale*, 7(30):12851–12859, 2015.

[40] Denis L Nika, Alexandr I Cocemasov, and Alexander A Balandin. Specific heat of twisted bilayer graphene: Engineering phonons by atomic plane rotations. *Applied Physics Letters*, 105(3):031904, 2014.

[41] Haijun Huang, Jie Zhang, Lian Jiang, and Zhigang Zang. Preparation of cubic cu2o nanoparticles wrapped by reduced graphene oxide for the efficient removal of rhodamine b. *Journal of Alloys and Compounds*, 718:112–115, 2017.

[42] G Trambly de Laissardiere, Didier Mayou, and Laurence Magaud. Localization of dirac electrons in rotated graphene bilayers. *Nano letters*, 10(3):804–808, 2010.

[43] K. M. Masum Habib, Somaia S. Sylvia, Supeng Ge, Mahesh Neupane, and Roger K. Lake. The coherent interlayer resistance of a single, rotated interface between two stacks of ab graphite. *Appl. Phys. Lett.*, 103(24):243114, 2013.

[44] William J Evans, Lin Hu, and Pawel Keblinski. Thermal conductivity of graphene ribbons from equilibrium molecular dynamics: Effect of ribbon width, edge roughness, and hydrogen termination. *Applied Physics Letters*, 96(20):203112, 2010.

[45] Steve Plimpton, Paul Crozier, and Aidan Thompson. Lammps-large-scale atomic/-molecular massively parallel simulator. *Sandia National Laboratories*, 18:43–43, 2007.

[46] Donald W Brenner, Olga A Shenderova, Judith A Harrison, Steven J Stuart, Boris Ni, and Susan B Sinnott. A second-generation reactive empirical bond order (rebo) potential energy expression for hydrocarbons. *Journal of Physics: Condensed Matter*, 14(4):783, 2002.

[47] Irina V Lebedeva, Andrey A Knizhnik, Andrey M Popov, Yurii E Lozovik, and Boris V Potapkin. Interlayer interaction and relative vibrations of bilayer graphene. *Physical Chemistry Chemical Physics*, 13(13):5687–5695, 2011.

[48] A Maiti, GD Mahan, and ST Pantelides. Dynamical simulations of nonequilibrium processes—heat flow and the kapitza resistance across grain boundaries. *Solid state communications*, 102(7):517–521, 1997.

[49] Florian Müller-Plathe. A simple nonequilibrium molecular dynamics method for calculating the thermal conductivity. *The Journal of chemical physics*, 106(14):6082–6085, 1997.

[50] Wei-Rong Zhong, Mao-Ping Zhang, Bao-Quan Ai, and Dong-Qin Zheng. Chirality and thickness-dependent thermal conductivity of few-layer graphene: A molecular dynamics study. *Applied Physics Letters*, 98(11):113107, 2011.

[51] John M Ziman. *Electrons and phonons: the theory of transport phenomena in solids.* Oxford university press, 1960.

[52] Keith T Regner, Daniel P Sellan, Zonghui Su, Cristina H Amon, Alan JH McGaughey, and Jonathan A Malen. Broadband phonon mean free path contributions to thermal conductivity measured using frequency domain thermoreflectance. *Nature communications*, 4:1640, 2013.

[53] ZhengXing Huang and ZhenAn Tang. Evaluation of momentum conservation influence in non-equilibrium molecular dynamics methods to compute thermal conductivity. *Physica B: Condensed Matter*, 373(2):291–296, 2006.

[54] Ling Ti Kong. Phonon dispersion measured directly from molecular dynamics simulations. *Computer Physics Communications*, 182(10):2201–2207, 2011.

[55] Mahesh Raj Neupane. *Electronic and Vibrational Properties of Low-Dimensional Heterogeneous Systems: Materials and Device Perspectives.* PhD thesis, University of California, Riverside, 2015.

[56] Wu Li, Jesús Carrete, Nebil A Katcho, and Natalio Mingo. Shengbte: A solver of the boltzmann transport equation for phonons. *Computer Physics Communications*, 185(6):1747–1758, 2014.

[57] Rafi Bistritzer and Allan H MacDonald. Transport between twisted graphene layers. *Physical Review B*, 81(24):245412, 2010.

[58] V. Perebeinos, J. Tersoff, and P. Avouris. Phonon-mediated interlayer conductance in twisted graphene bilayers. *Phys. Rev. Lett.*, 109(23):236604, 2012.

[59] Tarun Chari, Rebeca Ribeiro-Palau, Cory R. Dean, and Kenneth Shepard. Resistivity of rotated graphite–graphene contacts. *Nano Letters*, 16(7):4477–4482, 2016.

[60] Patrick K Schelling, Simon R Phillpot, and Pawel Keblinski. Comparison of atomic-level simulation methods for computing thermal conductivity. *Physical Review B*, 65(14):144306, 2002.

[61] L Lindsay, DA Broido, and Natalio Mingo. Flexural phonons and thermal transport in graphene. *Physical Review B*, 82(11):115427, 2010.

[62] Minkyu Park, Sun-Chul Lee, and Yong-Sung Kim. Length-dependent lattice thermal conductivity of graphene and its macroscopic limit. *Journal of Applied Physics*, 114(5):053506, 2013.

[63] Savas Berber, Young-Kyun Kwon, and David Tománek. Unusually high thermal conductivity of carbon nanotubes. *Physical review letters*, 84(20):4613, 2000.

[64] Denis L Nika and Alexander A Balandin. Phonons and thermal transport in graphene and graphene-based materials. *Reports on Progress in Physics*, 80(3):036502, 2017.

[65] John P Perdew, Kieron Burke, and Matthias Ernzerhof. Generalized gradient approximation made simple. *Physical review letters*, 77(18):3865, 1996.

[66] Georg Kresse and Jürgen Furthmüller. Efficiency of ab-initio total energy calculations for metals and semiconductors using a plane-wave basis set. *Computational materials science*, 6(1):15–50, 1996.

[67] Georg Kresse and J Hafner. Ab initio molecular dynamics for open-shell transition metals. *Physical Review B*, 48(17):13115, 1993.

[68] Stefan Grimme. Semiempirical gga-type density functional constructed with a long-range dispersion correction. *Journal of computational chemistry*, 27(15):1787–1799, 2006.

[69] Tomas Bučko, Jurgen Hafner, Sébastien Lebègue, and János G Ángyán. Improved description of the structure of molecular and layered crystals: ab initio dft calculations with van der waals corrections. *The Journal of Physical Chemistry A*, 114(43):11814–11824, 2010.

[70] Alfonso Reina, Xiaoting Jia, John Ho, Daniel Nezich, Hyungbin Son, Vladimir Bulovic, Mildred S Dresselhaus, and Jing Kong. Large area, few-layer graphene films on arbitrary substrates by chemical vapor deposition. *Nano letters*, 9(1):30–35, 2008.

[71] Atsushi Togo and Isao Tanaka. First principles phonon calculations in materials science. *Scripta Materialia*, 108:1–5, 2015.

[72] Eugene J Mele. Commensuration and interlayer coherence in twisted bilayer graphene. *Physical Review B*, 81(16):161405, 2010.

[73] S Shallcross, S Sharma, E Kandelaki, and OA Pankratov. Electronic structure of turbostratic graphene. *Physical Review B*, 81(16):165105, 2010.

[74] E. Suárez Morell, J. D. Correa, P. Vargas, M. Pacheco, and Z. Barticevic. Flat bands in slightly twisted bilayer graphene: Tight-binding calculations. *Phys. Rev. B*, 82:121407, Sep 2010.

[75] R. Bistritzer and A. H. MacDonald. Moiré bands in twisted double-layer graphene. *Proceedings of the National Academy of Sciences*, 108(30):12233–12237, 2011.

[76] E. Koren, I. Leven, E. Lörtscher, A. Knoll, O. Hod, and U. Duerig. Coherent commensurate electronic states at the interface between misoriented graphene layers. *Nature nanotechnology*, 11(9):752, 2016.

[77] Z. Song, Z. Wang, W. Shi, G. Li, C. Fang, and B. A. Bernevig. All magic angles in twisted bilayer graphene are topological. *Physical review letters*, 123(3):036401, 2019.

[78] Yuan Cao, Valla Fatemi, Shiang Fang, Kenji Watanabe, Takashi Taniguchi, Efthimios Kaxiras, and Pablo Jarillo-Herrero. Unconventional superconductivity in magic-angle graphene superlattices. *Nature*, 556(7699):43, 2018.

[79] M. Yankowitz, S. Chen, H. Polshyn, Y. Zhang, K. Watanabe, T. Taniguchi, D. Graf, A. F. Young, and Cory R. Dean. Tuning superconductivity in twisted bilayer graphene. *Science*, 363(6431):1059–1064, 2019.

[80] B. Lian, Z. Wang, and B. A. Bernevig. Twisted bilayer graphene: A phonon-driven superconductor. *Phys. Rev. Lett.*, 122:257002, Jun 2019.

[81] R. Mao, Y. Chen, and K. W. Kim. Atomistic modeling of phonon transport in turbostratic graphitic structures. *Journal of Applied Physics*, 119(20):204305, 2016.

[82] Xianhua Nie, Li Zhao, Shuai Deng, Yue Zhang, and Zhenyu Du. How interlayer twist angles affect in-plane and cross-plane thermal conduction of multilayer graphene: A non-equilibrium molecular dynamics study. *International Journal of Heat and Mass Transfer*, 137:161–173, 2019.

[83] Emmanuel N Koukaras, George Kalosakas, Costas Galiotis, and Konstantinos Papagelis. Phonon properties of graphene derived from molecular dynamics simulations. *Scientific reports*, 5:12923, 2015.

[84] J Tersoff. Modeling solid-state chemistry: Interatomic potentials for multicomponent systems. *Physical Review B*, 39(8):5566, 1989.

[85] L Lindsay and DA Broido. Optimized tersoff and brenner empirical potential parameters for lattice dynamics and phonon thermal transport in carbon nanotubes and graphene. *Physical Review B*, 81(20):205441, 2010.

[86] D. W. Brenner. Empirical potential for hydrocarbons for use in simulating the chemical vapor deposition of diamond films. *Physical review B*, 42(15):9458, 1990.

[87] Steven J Stuart, Alan B Tutein, and Judith A Harrison. A reactive potential for hydrocarbons with intermolecular interactions. *The Journal of chemical physics*, 112(14):6472–6486, 2000.

[88] JH Los and A Fasolino. Intrinsic long-range bond-order potential for carbon: Performance in monte carlo simulations of graphitization. *Physical Review B*, 68(2):024107, 2003.

[89] GC Abell. Empirical chemical pseudopotential theory of molecular and metallic bonding. *Physical Review B*, 31(10):6184, 1985.

[90] Mingjian Wen, Stephen Carr, Shiang Fang, Efthimios Kaxiras, and Ellad B Tadmor. Dihedral-angle-corrected registry-dependent interlayer potential for multilayer graphene structures. *Physical Review B*, 98(23):235404, 2018.

[91] C Wang, Y Liu, L Li, and H Tan. Anisotropic thermal conductivity of graphene wrinkles. *Nanoscale*, 6(11):5703–5707, 2014.

[92] Dhruv Singh, Jayathi Y Murthy, and Timothy S Fisher. Mechanism of thermal conductivity reduction in few-layer graphene. *Journal of Applied Physics*, 110(4):044317, 2011.

[93] P. H. Tan, W. P. Han, W. J. Zhao, Z. H. Wu, K. Chang, H. Wang, Y. F. Wang, N. Bonini, N. Marzari, N. Pugno, G. Savini, A. Lombardo, and A. C. Ferrari. The shear mode of multilayer graphene. *Nature Materials*, 11(4):294–300, 2012.

[94] Shanshan Chen, Qiongyu Li, Qimin Zhang, Yan Qu, Hengxing Ji, Rodney S Ruoff, and Weiwei Cai. Thermal conductivity measurements of suspended graphene with and without wrinkles by micro-raman mapping. *Nanotechnology*, 23(36):365701, 2012.

[95] Annalisa Fasolino, JH Los, and Mikhail I Katsnelson. Intrinsic ripples in graphene. *Nature materials*, 6(11):858, 2007.

[96] G Savini, YJ Dappe, Sven Öberg, J-C Charlier, MI Katsnelson, and A Fasolino. Bending modes, elastic constants and mechanical stability of graphitic systems. *Carbon*, 49(1):62–69, 2011.

[97] Alexey Bosak, Michael Krisch, Marcel Mohr, Janina Maultzsch, and Christian Thomsen. Elasticity of single-crystalline graphite: Inelastic x-ray scattering study. *Phys. Rev. B*, 75:153408, Apr 2007.

[98] O. L. Blakslee, D. G. Proctor, E. J. Seldin, G. B. Spence, and T. Weng. Elastic constants of compressionannealed pyrolytic graphite. *Journal of Applied Physics*, 41(8):3373–3382, 1970.

[99] Jerry Tersoff. New empirical approach for the structure and energy of covalent systems. *Physical Review B*, 37(12):6991, 1988.

[100] Y Magnin, GD Förster, F Rabilloud, F Calvo, A Zappelli, and C Bichara. Thermal expansion of free-standing graphene: benchmarking semi-empirical potentials. *Journal of Physics: Condensed Matter*, 26(18):185401, 2014.

[101] Gowoon Cheon, Karel-Alexander N Duerloo, Austin D Sendek, Chase Porter, Yuan Chen, and Evan J Reed. Data mining for new two-and one-dimensional weakly bonded solids and lattice-commensurate heterostructures. *Nano letters*, 17(3):1915–1923, 2017.

[102] IM Lifshitz. Thermal properties of chain and layered structures at low temperatures. *Zh. Eksp. Teor. Fiz*, 22(4):475–486, 1952.

[103] Takeshi Nihira and Tadao Iwata. Temperature dependence of lattice vibrations and analysis of the specific heat of graphite. *Phys. Rev. B*, 68:134305, Oct 2003.

[104] K.Komatsu and T. Nagamiya. Theory of the specific heat of graphite. *J. Phys. Soc. Japan*, 6(6):438–444, 1951.

[105] K. Komatsu. Theory of specific heat in graphite ii. *J. Phys. Soc. Jap.*, 10(5):346–356, 1955.

[106] DL Nika, S Ghosh, EP Pokatilov, and AA Balandin. Lattice thermal conductivity of graphene flakes: Comparison with bulk graphite. *Applied Physics Letters*, 94(20):203103, 2009.

[107] Zhixin Guo, Dier Zhang, and Xin-Gao Gong. Thermal conductivity of graphene nanoribbons. *Applied physics letters*, 95(16):163103, 2009.

[108] Khan MF Shahil and Alexander A Balandin. Thermal properties of graphene and multilayer graphene: Applications in thermal interface materials. *Solid State Communications*, 152(15):1331–1340, 2012.

[109] Zongyou Yin, Jixin Zhu, Qiyuan He, Xiehong Cao, Chaoliang Tan, Hongyu Chen, Qingyu Yan, and Hua Zhang. Graphene-based materials for solar cell applications. *Advanced energy materials*, 4(1):1300574, 2014.

[110] Weiwei Li, Xiumei Geng, Yufen Guo, Jizan Rong, Youpin Gong, Liqiong Wu, Xuemin Zhang, Peng Li, Jianbao Xu, Guosheng Cheng, et al. Reduced graphene oxide electrically contacted graphene sensor for highly sensitive nitric oxide detection. *ACS nano*, 5(9):6955–6961, 2011.

[111] Hyeun Joong Yoon, Jin Ho Yang, Zhixian Zhou, Sang Sik Yang, Mark Ming-Cheng Cheng, et al. Carbon dioxide gas sensor using a graphene sheet. *Sensors and Actuators B: Chemical*, 157(1):310–313, 2011.

[112] Marcus A Worsley, Peter J Pauzauskie, Tammy Y Olson, Juergen Biener, Joe H Satcher Jr, and Theodore F Baumann. Synthesis of graphene aerogel with high electrical conductivity. *Journal of the American Chemical Society*, 132(40):14067–14069, 2010.

[113] Hyunwoo Kim, Yutaka Miura, and Christopher W Macosko. Graphene/polyurethane nanocomposites for improved gas barrier and electrical conductivity. *Chemistry of materials*, 22(11):3441–3450, 2010.

[114] Haiqun Chen, Marc B Müller, Kerry J Gilmore, Gordon G Wallace, and Dan Li. Mechanically strong, electrically conductive, and biocompatible graphene paper. *Advanced Materials*, 20(18):3557–3561, 2008.

[115] Sasha Stankovich, Dmitriy A Dikin, Geoffrey HB Dommett, Kevin M Kohlhaas, Eric J Zimney, Eric A Stach, Richard D Piner, SonBinh T Nguyen, and Rodney S Ruoff. Graphene-based composite materials. *nature*, 442(7100):282, 2006.

[116] Jae Hun Seol, Insun Jo, Arden L Moore, Lucas Lindsay, Zachary H Aitken, Michael T Pettes, Xuesong Li, Zhen Yao, Rui Huang, David Broido, et al. Two-dimensional phonon transport in supported graphene. *Science*, 328(5975):213–216, 2010.

[117] Andrea C Ferrari. Raman spectroscopy of graphene and graphite: disorder, electron–phonon coupling, doping and nonadiabatic effects. *Solid state communications*, 143(1-2):47–57, 2007.

[118] Andrea C Ferrari, JC Meyer, V Scardaci, C Casiraghi, Michele Lazzeri, Francesco Mauri, S Piscanec, Da Jiang, KS Novoselov, S Roth, et al. Raman spectrum of graphene and graphene layers. *Physical review letters*, 97(18):187401, 2006.

[119] Anindya Das, Simone Pisana, Biswanath Chakraborty, Stefano Piscanec, Srijan K Saha, Umesh V Waghmare, Konstantin S Novoselov, Hulikal R Krishnamurthy, Andre K Geim, Andrea C Ferrari, et al. Monitoring dopants by raman scattering in an electrochemically top-gated graphene transistor. *Nature nanotechnology*, 3(4):210, 2008.

[120] Wen Hui Duan, Kai Gong, and Quan Wang. Controlling the formation of wrinkles in a single layer graphene sheet subjected to in-plane shear. *Carbon*, 49(9):3107–3112, 2011.

[121] Changguo Wang, Yuanpeng Liu, Lan Lan, and Huifeng Tan. Graphene wrinkling: formation, evolution and collapse. *Nanoscale*, 5(10):4454–4461, 2013.

[122] K Min and Narayana R Aluru. Mechanical properties of graphene under shear deformation. *Applied Physics Letters*, 98(1):013113, 2011.

[123] Changguo Wang, Lan Lan, and Huifeng Tan. The physics of wrinkling in graphene membranes under local tension. *Physical Chemistry Chemical Physics*, 15(8):2764–2773, 2013.

[124] Qingzhi Wu, Yaping Wu, Yufeng Hao, Jianxin Geng, Matthew Charlton, Shanshan Chen, Yujie Ren, Hengxing Ji, Huifeng Li, Danil W Boukhvalov, et al. Selective surface functionalization at regions of high local curvature in graphene. *Chemical Communications*, 49(7):677–679, 2012.

[125] Zacharias G. Fthenakis, Zhen Zhu, and David Tománek. Effect of structural defects on the thermal conductivity of graphene: From point to line defects to haeckelites. *Phys. Rev. B*, 89:125421, Mar 2014.

[126] Savas Berber, Young-Kyun Kwon, and David Tománek. Unusually high thermal conductivity of carbon nanotubes. *Phys. Rev. Lett.*, 84:4613–4616, May 2000.

[127] Patrick K. Schelling, Simon R. Phillpot, and Pawel Keblinski. Comparison of atomic-level simulation methods for computing thermal conductivity. *Phys. Rev. B*, 65:144306, Apr 2002.

[128] Denis L Nika and Alexander A Balandin. Two-dimensional phonon transport in graphene. *Journal of Physics: Condensed Matter*, 24(23):233203, 2012.

[129] Jan H Los, Luca M Ghiringhelli, Evert Jan Meijer, and A Fasolino. Improved long-range reactive bond-order potential for carbon. i. construction. *Physical Review B*, 72(21):214102, 2005.

[130] Robert M Elder, Mahesh R Neupane, and Tanya L Chantawansri. Stacking order dependent mechanical properties of graphene/mos2 bilayer and trilayer heterostructures. *Applied Physics Letters*, 107(7):073101, 2015.

[131] Mahesh Raj Neupane. *Electronic and Vibrational Properties of Low-Dimensional Heterogeneous Systems: Materials and Device Perspectives.* University of California, Riverside, 2015.

[132] Austin J Minnich, JA Johnson, AJ Schmidt, Keivan Esfarjani, MS Dresselhaus, Keith A Nelson, and Gang Chen. Thermal conductivity spectroscopy technique to measure phonon mean free paths. *Physical review letters*, 107(9):095901, 2011.

[133] Pilkyung Moon and Mikito Koshino. Optical absorption in twisted bilayer graphene. *Physical Review B*, 87(20):205404, 2013.

[134] Qinghong Yuan, Boris I Yakobson, and Feng Ding. Edge-catalyst wetting and orientation control of graphene growth by chemical vapor deposition growth. *The journal of physical chemistry letters*, 5(18):3093–3099, 2014.

[135] Laszlo P Biro and Philippe Lambin. Nanopatterning of graphene with crystallographic orientation control. *Carbon*, 48(10):2677–2689, 2010.

[136] Adrian T Murdock, Antal Koos, T Ben Britton, Lothar Houben, Tim Batten, Tong Zhang, Angus J Wilkinson, Rafal E Dunin-Borkowski, Christina E Lekka, and Nicole Grobert. Controlling the orientation, edge geometry, and thickness of chemical vapor deposition graphene. *Acs Nano*, 7(2):1351–1359, 2013.

[137] PG Klemens. Theory of the a-plane thermal conductivity of graphite. *Thermal Conductivity*, 22:365–365, 1993.